DRAFT VERSION JANUARY 27, 2015
Preprint typeset using LaTeX style emulateapj v. 08/13/06

arXiv:1501.06210v1 [astro-ph.SR] 25 Jan 2015

PROBING STELLAR ACCRETION WITH MID-INFRARED HYDROGEN LINES

ELISABETTA RIGLIACO [1]
Department of Planetary Science, University of Arizona, 1629 E. University Blvd. Tucson, AZ 85719, USA and
Institute for Astronomy, ETH Zurich, Wolfgang-Pauli-Strasse 27, CH-8093 Zurich, Switzerland

I. PASCUCCI
Department of Planetary Science, University of Arizona, 1629 E. University Blvd. Tucson, AZ 85719, USA

G. DUCHENE
Astronomy Department, University of California, Berkeley, Hearst Field Annex B-20, Berkeley CA 94720-3411, USA
Universite de Grenoble Alpes, IPAG, F-38000 Grenoble, France and
CNRS, IPAG, F-38000 Grenoble, France

S. EDWARDS
Five College Astronomy Department, Smith College, Northampton, MA 01063, USA

D.R. ARDILA
NASA Herschel Science Center, California Institute of Technology, MC 100-22, Pasadena, CA 91125, USA and
The Aerospace Corporation, M2-266, El Segundo, CA 90245, USA

C. GRADY
Eureka Scientific,2452 Delmer Street, Suite 100 Oakland, CA 94602-3017 and
Exoplanets and Stellar Astrophysics Lab, Code 667, GoddardSpace Flight Center, Greenbelt, MD 20771

I. MENDIGUTÍA
School of Physics and Astronomy, University of Leeds, Woodhouse Lane, Leeds LS2 9JT, UK

B. MONTESINOS
Departamento de Astrofísica, Centro de Astrobiología, ESAC Campus, PO Box 78, 28691 Villanueva de la Cañada, Madrid, Spain

G. D. MULDERS
Department of Planetary Science, University of Arizona, 1629 E. University Blvd. Tucson, AZ 85719, USA

J.R. NAJITA
National Optical Astronomy Observatory, 950 North Cherry Avenue, Tucson, AZ 85719, USA

J. CARPENTER
Department of Astronomy, California Institute of Technology, MC 249-17, Pasadena, CA 91125, USA

E. FURLAN
Infrared Processing and Analysis Center, California Institute of Technology, 770 S. Wilson Ave., Pasadena, CA 91125, USA.

U. GORTI
NASA Ames Research Center, Moffett Field, CA, USA and
SETI Institute, Mountain View, CA, USA

R. MEIJERINK
Leiden Observatory, Leiden University, P.O. Box 9513, NL-2300 RA, Leiden, The Netherlands

M.R. MEYER
Institute for Astronomy, ETH Zurich, Wolfgang-Pauli-Strasse 27, CH-8093 Zurich, Switzerland
Draft version January 27, 2015

ABSTRACT

In this paper we investigate the origin of the mid-infrared (IR) hydrogen recombination lines for a sample of 114 disks in different evolutionary stages (full, transitional and debris disks) collected from the *Spitzer* archive. We focus on the two brighter H I lines observed in the *Spitzer* spectra, the H I(7-6) at 12.37μm and the H I(9-7) at 11.32μm. We detect the H I(7-6) line in 46 objects, and the H I(9-7) in 11. We compare these lines with the other most common gas line detected in *Spitzer* spectra, the [Ne II] at 12.81μm. We argue that it is unlikely that the H I emission originates from the photoevaporating upper surface layers of the disk, as has been found for the [Ne II] lines toward low-accreting stars. Using the H I(9-7)/H I(7-6) line ratios we find these gas lines are likely probing gas with hydrogen column densities of 10^{10}-10^{11} cm^{-3}. The subsample of objects surrounded by full and transitional disks show a positive correlation between the accretion luminosity and the H I line luminosity. These two results suggest that the observed mid-IR H I lines trace gas accreting onto the star in the same way as other hydrogen recombination lines at shorter wavelengths. A pure chromospheric origin of these lines can be excluded for the vast majority of full and transitional disks. We report for the first time the detection of the H I(7-6) line in eight young (< 20 Myr) debris disks. A pure chromospheric origin cannot be ruled out in these objects. If the H I(7-6) line traces accretion in these older systems, as in the case of full and transitional disks, the strength of the emission implies accretion rates lower than 10^{-10}M$_\odot$/yr. We discuss some advantages of extending accretion indicators to longer wavelengths, and the next steps required to pin down the origin of mid-infrared hydrogen lines.

Subject headings: accretion, accretion disks — circumstellar matter — infrared: stars — line: identification — stars: activity

1. INTRODUCTION

The analysis and characterization of circumstellar disks, which provide the raw material to form planets, are crucial for our understanding of disk dispersal and planet formation processes. Observations and modeling of the dust content in protoplanetary disks are nowadays relatively abundant (see Testi et al. 2014 for a review). The gaseous component of circumstellar disks is instead less well characterized (e.g., Dutrey et al. 2014 for a review) even if major advances have been made in the past few years thanks to space observatories such as *Spitzer* (e.g., Pontoppidan et al. 2014) and *Herschel* (e.g., Dent et al. 2013). Gas plays a pivotal role in the structure and evolution of disks representing the bulk of the disk mass (e.g., Alexander et al. 2014). It is then necessary to extend our knowledge of the disk gas content in order to improve our understanding of the natal environments of planets.

The sensitivity of the InfraRed Spectrograph (IRS) on the *Spitzer* Space Telescope led to the discovery of gas lines that can be used to characterize the immediate surroundings of young stellar objects (YSOs). For instance, the rich water spectrum of YSOs has been attributed to emission arising from warm ($\sim$600 K) layers of water vapor out to a few AUs from the central star (Carr & Najita 2008, 2011, Salyk et al. 2008, Pontoppidan et al. 2010, Salyk et al. 2011, Banzatti et al. 2013).

Among the wide forest of lines revealed by *Spitzer* the most common one is the singly ionized neon, [Ne II] at 12.81μm (e.g., Pascucci et al. 2007, Lahuis et al 2007, Güdel et al. 2010). Different studies of this line show that objects with known jets/outflows have higher [Ne II] luminosity than objects without (Güdel et al. 2010, Baldovin-Saavedra et al. 2011). Moreover, follow up observations of this line with ground-based high-resolution spectrographs have shown that [Ne II] is predominantly tracing an outflow in high-accreting stars, while its origin is from photoevaporative disk winds driven by high-energy photons from the central star in lower accretors (Pascucci & Sterzik 2009, van Boekel et al. 2009, Sacco et al. 2012, Baldovin-Saavedra et al. 2012).

Other gas lines that are commonly used to characterize objects undergoing accretion are hydrogen recombination lines. H I lines from the near-ultraviolet (UV) to the near-infrared (IR) have been extensively used as indicators of the rate at which the matter from the inner circumstellar disk is accreting onto the star (e.g., Muzerolle et al. 2001, Calvet et al. 2004, Natta et al. 2006, Alcalà et al. 2014, Edwards et al. 2013 among many others). Recently, Salyk et al. (2013) using NIRSPEC at the Keck II telescope and CRIRES at the Very Large Telescope have introduced the H I Pfβ line at 4.65μm as accretion diagnostic. This is to date the longest wavelength hydrogen line proposed as accretion indicator.

As early as 2007, Pascucci et al. (2007) reported also the detection of H I lines in the *Spitzer* spectrum of RX1852.3-3700. Subsequently, Ratzka et al. (2007) and Najita et al. (2010) reported hydrogen line detections in both the low- and high-resolution *Spitzer* spectrum of TWHya. The analysis of these two objects did not constrain the origin of these lines and left several possibilities open: stellar chromosphere, hot disk atmosphere, accretion shock regions, or internal wind shock very close to the stellar surface (Hollenbach & Gorti 2009). More recently, Carr & Najita (2011) reported the detection of the IR hydrogen lines in 10 T Tauri stars but did not discuss their origin.

Here, we improve upon studies of gas lines from circumstellar disks by analyzing hydrogen lines observed in the *Spitzer*/IRS spectra of a large sample of objects. In particular we focus on the strongest of the Humphreys Series lines in the mid-infrared, the Huα at 12.37μm (hereafter H I(7-6)) and the H I(9-7) line at 11.32μm. With the aim to investigate the origin of these mid-IR hydrogen lines, we compare their properties both with hydrogen lines observed at shorter wavelengths, mainly tracing accretion, and with the other most common gas line observed in the *Spitzer* spectra ([Ne II]) which is instead an outflow or disk wind tracer depending on the mass accretion rate.

The paper is organized as follows. In Section 2 the source selection and data reduction are explained. In Section 3 we describe the method used to account for the water contamination of the H I lines, and how we measure the H I and [Ne II] line fluxes and luminosities. In Section 4 we discuss the origin of the H I mid-IR lines, highlighting the interesting presence of H I lines in a sample of debris disks. The summary of the results and an outlook are given in Section 5.

2. SAMPLE SELECTION AND DATA REDUCTION

Electronic address: [1]rigliaco@lpl.arizona.edu, elisabetta.rigliaco@phys.ethz.ch

Using the *Spitzer* Heritage Archive[1] we downloaded and re-reduced all IRS Short-High (SH) spectra of disks-bearing young stars acquired in the Standard Staring Mode and which have multiple on-source exposures (N-cycle >1) and sky observations. The latter two restrictions were applied to better identify and correct for bad pixels as summarized below. A list of the 114 objects identified in this way and with a signal-to-noise on the continuum greater than 5 is reported in Table 1. This table also contains the source coordinates, the Astronomical Observation Request number (AOR), the Identification Number (ID) of the *Spitzer* program the object belongs to, and the exposure time per frame times the number of exposures. We also report in Table A1 the sources' properties, and in Table A2 the mid-IR line fluxes, errors and continuum levels around the three line of interest.

[1] http://sha.ipac.caltech.edu/applications/Spitzer/SHA/

TABLE 1
ALL OBJECTS REDUCED: OBSERVING LOG

Name	RA	DEC	AOR	Program ID	Time×Ncycles
HD 377	0h08m25.76s	+6d37m00.3s	13462272	148	120 × 3
HD 12039	1h57m48.97s	-21d54m05.2s	13461760	148	120 × 4
HD 17925	2h52m32.13s	-12d46m11.0s	9780480	148	30 × 5
HD 19668	3h09m42.28s	-9d34m46.4s	13462784	148	120 × 3
LkHa 326	3h30m44.01s	+30d32m47.0s	27063552	50641	30 × 12
IC348-67	3h43m44.62s	+32d08m17.9s	22850816	40247	30 × 100
IC348-31	3h44m18.16s	+32d04m57.0s	22849280	40247	30 × 16
IC348-72	3h44m22.58s	+32d01m53.7s	22851840	40247	30 × 100
IC348-68	3h44m28.51s	+31d59m54.1s	22851328	40247	30 × 100
IC348-55	3h44m31.36s	+32d00m14.7s	22850304	40247	30 × 80
IC348-2	3h44m35.36s	+32d10m04.6s	22847744	40247	30 × 4
IC348-6	3h44m36.94s	+32d06m45.4s	22848256	40247	30 × 16
IC348-37	3h44m37.99s	+32d03m29.8s	22849792	40247	30 × 30
IC348-133	3h44m41.74s	+32d12m02.4s	22852352	40247	30 × 100
IC348-21	3h44m56.15s	+32d09m15.5s	22848768	40247	30 × 30
LkHa 330	3h45m48.28s	+32d24m11.9s	27063040	50641	30 × 7
HD 25457	4h02m36.74s	-0d16m08.1s	9779712	148	6 × 4
FM Tau	4h14m13.58s	+28d12m49.3s	24403968	30300	120 × 2
FN Tau	4h14m14.59s	+28d27m58.0s	27062528	50641	30 × 6
CW Tau	4h14m17.00s	+28d10m57.8s	27062272	50641	30 × 6
FP Tau	4h14m47.30s	+26d46m26.4s	26321408	50498	30 × 8
CX Tau	4h14m47.86s	+26d48m11.0s	23551744	40338	30 × 21
CY Tau	4h17m33.72s	+28d20m46.8s	27061504	50641	30 × 14
DD Tau	4h18m31.13s	+28d16m28.9s	26320384	50498	30 × 2
BP Tau	4h19m15.84s	+29d06m27.0s	14548224	20363	30 × 12
DE Tau	4h21m55.67s	+27d55m06.2s	27060992	50641	30 × 10
FT Tau	4h23m39.18s	+24d56m14.3s	27060224	50641	30 × 14
04216+2603	4h24m44.58s	+26d10m14.2s	27059968	50641	30 × 12
IP Tau	4h24m57.08s	+27d11m56.3s	24404224	30300	120 × 5
DG Tau	4h27m04.70s	+26d06m15.8s	14547968	20363	6 × 12
DH Tau	4h29m41.57s	+26d32m58.2s	26320128	50498	30 × 10
UX TauA	4h30m04.00s	+18d13m49.4s	18013952	30300	30 × 30
DK Tau	4h30m44.28s	+26d01m24.6s	14548736	20363	30 × 8
HK Tau	4h31m50.58s	+24d24m17.8s	27059200	50641	30 × 14
FZ Tau	4h32m31.77s	+24d20m02.6s	27058688	50641	30 × 6
HN Tau	4h33m39.36s	+17d51m52.3s	27058176	50641	30 × 6
DL Tau	4h33m39.08s	+25d20m38.1s	27058432	50641	30 × 6
DM Tau	4h33m48.72s	+18d10m10.0s	18014720	30300	30 × 30
AA Tau	4h34m55.44s	+24d28m53.4s	14551552	20363	30 × 12
DN Tau	4h35m27.37s	+24d14m58.9s	24404480	30300	30 × 9
DO Tau	4h38m28.58s	+26d10m49.4s	14548480	20363	30 × 8
LkCa 15	4h39m17.80s	+22d21m03.5s	23551488	40338	30 × 21
04385+2550	4h41m38.82s	+25d56m27.0s	27057408	50641	30 × 6
DP Tau	4h42m37.69s	+25d15m37.3s	27057152	50641	30 × 6
DQ Tau	4h46m53.06s	+17d00m00.4s	26321152	50498	30 × 2
DR Tau	4h47m06.22s	+16d58m42.9s	27067136	50641	6 × 12
DS Tau	4h47m48.60s	+29d25m11.6s	26320896	50498	30 × 4
UY Aur	4h51m47.38s	+30d47m13.9s	14551040	20363	6 × 10
St 34	4h54m23.68s	+17d09m53.5s	18016256	30300	30 × 40
GM Aur	4h55m10.98s	+30d21m59.5s	18015488	30300	30 × 10
SU Aur	4h55m59.38s	+30d34m01.5s	27066880	50641	6 × 10
HD 32297	5h02m27.44s	+7d27m39.7s	25677568	50150	30 × 5
V836 Tau	5h03m06.60s	+25d23m19.7s	23552000	40338	30 × 21
RW Aur	5h07m49.56s	+30d24m05.0s	14547200	20363	6 × 13
HD 35850	5h27m04.76s	-11d54m03.5s	9777920	148	30 × 6
HD 37484	5h37m39.62s	-28d37m34.7s	9780224	148	30 × 10
NGC2068/ 2071-H9	5h46m11.86s	+0d32m25.9s	22853888	40247	30 × 100
NGC2068/ 2071-S1	5h46m18.89s	-0d05m38.2s	22854912	40247	30 × 50
NGC2068/ 2071-H13	5h46m22.44s	-0d08m52.6s	22854400	40247	30 × 80
AO Men	6h18m28.24s	-72d02m41.7s	5458688	148	120 × 2
HD 61005	7h35m47.47s	-32d12m14.2s	13462528	148	120 × 3

TABLE 1 — *Continued*

Name	RA	DEC	AOR	Program ID	Time×Ncycles
HD 69830	8h18m23.95s	-12d37m55.8s	12710656	41	30 × 2
SX Cha	10h55m59.76s	-77d24m40.1s	27066624	50641	30 × 7
TW Cha	10h56m30.52s	-77d11m39.4s	27066368	50641	30 × 28
SZ Cha	10h58m16.77s	-77d17m17.1s	22846208	40247	30 × 4
TW Hya	11h01m51.91s	-34d42m17.0s	18017792	30300	30 × 2
CS Cha	11h02m24.91s	-77d33m35.7s	18021632	30300	30 × 50
Ced110-IRS2	11h06m15.41s	-77d21m56.8s	18022400	30300	30 × 10
Ced110-IRS4	11h06m46.58s	-77d22m32.6s	18019328	30300	30 × 36
Sz 18	11h07m19.15s	-76d03m04.8s	18020864	30300	30 × 100
VW Cha	11h08m01.47s	-77d42m28.7s	27066112	50641	30 × 6
Sz 27	11h08m39.05s	-77d16m04.2s	22847232	40247	30 × 100
VZ Cha	11h09m23.79s	-76d23m20.8s	27065856	50641	30 × 8
WX Cha	11h09m58.74s	-77d37m09.0s	27065600	50641	30 × 12
Hen 3-600A	11h10m27.53s	-37d31m53.6s	18018560	30300	30 × 2
XX Cha	11h11m39.66s	-76d20m15.3s	27065344	50641	30 × 14
RX J1111.7-7620	11h11m46.31s	-76d20m09.1s	5451776	148	30 × 6
CHX22	11h12m42.69s	-77d22m23.1s	22846720	40247	30 × 60
1RXS J121236.4-552037	12h12m35.77s	-55d20m27.4s	5460992	148	120 × 6
1RXS J122233.4-533347	12h22m33.23s	-53d33m48.9s	13463296	148	120 × 6
TWA 10	12h35m04.30s	-41d36m39.0s	22934528	40338	30 × 10
Sz 50	13h00m55.38s	-77d10m22.1s	27065088	50641	30 × 14
1RXS J130153.7-530446	13h01m50.69s	-53d04m58.1s	13462016	148	120 × 6
1RXS J132207.2-693812 (MPMus)	13h22m07.54s	-69d38m12.1s	5451264	148	6 × 3
1RXS J133758.0-413448	13h37m57.30s	-41d34m42.0s	5460224	148	120 × 6
HD 119269	13h43m28.54s	-54d36m43.5s	5461248	148	120 × 2
HD 134319	15h05m49.91s	+64d02m50.0s	9779968	148	30 × 6
V343Nor	15h38m57.56s	-57d42m27.3s	5458944	148	120 × 2
HT Lup	15h45m12.87s	-34d17m30.6s	27064832	50641	6 × 10
GQ Lup	15h49m12.11s	-35d39m04.8s	27064576	50641	30 × 8
HD 141943	15h53m27.30s	-42d16m00.8s	5462528	148	120 × 4
HD 142361	15h54m59.86s	-23d47m18.2s	5461504	148	120 × 12
IM Lup	15h56m09.21s	-37d56m05.9s	27064320	50641	30 × 6
RU Lup	15h56m42.31s	-37d49m15.5s	27064064	50641	30 × 5
HD 143006	15h58m36.93s	-22d57m15.4s	9777152	148	6 × 8
RX J1600.6-2159	16h00m40.57s	-22d00m32.3s	17145344	148	120 × 9
EX Lup	16h03m05.49s	-40d18m25.3s	27063808	50641	30 × 6
RX J1612.6-1859	16h12m40.51s	-18d59m28.3s	5457664	148	120 × 4
RXJS J161410.6-230542	16h14m11.08s	-23d05m36.2s	5453824	148	30 × 2
1RXS J161458.4-275013	16h14m59.17s	-27d50m23.0s	17144832	148	120 × 9
DoAr 21	16h26m03.03s	-24d23m36.4s	24403456	30300	30 × 6
DoAr 24E	16h26m23.42s	-24d21m00.5s	27062784	50641	30 × 5
DoAr 25	16h26m23.69s	-24d43m14.0s	24403712	30300	120 × 4
SR 21	16h27m10.20s	-24d19m16.0s	24403200	30300	6 × 10
Haro 1-16	16h31m33.46s	-24d27m37.4s	27062016	50641	30 × 7
RNO 90	16h34m09.17s	-15d48m16.8s	27061760	50641	6 × 9
WaOph6	16h48m45.63s	-14d16m36.0s	27060736	50641	30 × 6
EC 82	18h29m56.90s	+1d14m46.5s	27059712	50641	30 × 8
RX J1842.9-3532	18h42m57.97s	-35d32m42.7s	5451521	148	30 × 5
RX J1852.3-3700	18h52m17.30s	-37d00m11.9s	5452033	148	120 × 2
AS 353A	19h20m30.98s	+11d01m54.8s	14547456	20363	30 × 8
V1331 Cyg	21h01m09.20s	+50d21m44.5s	14547712	20363	30 × 8
HD 202917	21h20m49.96s	-53d02m03.2s	9778176	148	30 × 5
HD 216803	22h56m24.05s	-31d33m56.1s	9777664	148	30 × 5

The IRS SH module uses a cross-dispersed echelle design and covers the spectral range 9.9-19.6 μm with a nominal resolving power of R$\sim$600 (Houck et al. 2004). The data reduction was performed starting from the *droopres* products following the procedure outlined in Pascucci et al. (2013). In brief, we computed the average of the on-source and sky exposures per nod position and rejected bad pixels using the noise statistics from multiple cycles. We then created background subtracted images and corrected for the additional known bad pixels reported in the IRS BCD mask. The one dimensional spectrum was extracted from the background-subtracted pixel-corrected images using the full aperture extraction routine in SMART (Higdon et al. 2004). We applied the same procedure to our sources and to the *Spitzer* flux calibrator ξ Dra. From the reduction of 10 different exposures of ξ Dra and the known stellar model atmosphere we created two one-dimensional spectral response functions (one at each nod position). Finally, we divided the source spectra by the spectral response function. A compilation of four *Spitzer*/IRS SH spectra analyzed in this paper is shown in Figure 1.

The calibrated spectra of 54 sources belonging to the program IDs 40247, 20363, 148 and 41 can be downloaded from the IRSA Spitzer Science Center at *http://irsa.ipac.caltech.edu/data/SPITZER/Disks_SH_spectra*.

The total sample includes objects classified according to their general disk properties. We use the generic term Full Disks (F) for those disks with strong excess emission above photospheric levels at infrared wavelengths, starting in the near-IR. Transitional Disks (T) are broadly defined as disks with reduced near- and mid-IR excess fluxes but excess emission comparable to full disks beyond $\sim$20μm, indicative of a depleted inner region. Finally, Debris Disks (D) are de-

fined in this paper as having pure photosphere emission out to about 10 μm but can have relatively small excess emission in the long portion of the mid-IR spectrum. This disk classification collected from the literature is based on the dust properties and the continuum spectral energy distributions, and it is mainly taken from Furlan et al. (2006, 2011), Espaillat et al. (2012), Silverstone et al. (2006), Chen et al. (2014), as reported in Table A1. Most of the debris disks included in our study belong to the recent catalog published by Chen et al. (2014). Full and transitional disks are primordial, gas-rich disks, while debris disks are second-generation disks, dominated by dust. In total our sample includes 68 full, 21 transitional, and 25 debris disks. In Figure 2 we show the distribution in mass, luminosity, effective temperature and accretion luminosity (see Sect. 3.2) for the total sample, and for the objects where the H I(7-6) line is detected. A K-S two sample test of the stellar properties shows the two dataset have most likely the same parent distribution.

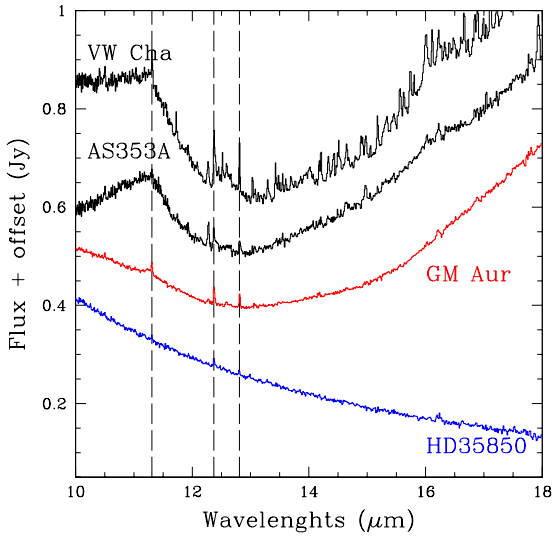

FIG. 1.— *Spitzer*/IRS SH spectra of four disks. For plotting purposes offsets have been applied as follows: -0.1 Jy at VWCha (water-contaminated full disk), -0.6 Jy at AS 353A (water-free full disk), +0.3 Jy at GM Aur (transitional disk) and 0.0 Jy at HD 35850 (debris disk). The vertical dashed lines show the location of the three lines mainly used through this paper: H I(7-6) at 12.37μm, H I(9-7) at 11.32μm and [Ne II] at 12.81μm.

3. ANALYSIS AND IMMEDIATE RESULTS

In the following, we summarize the main properties of our sample (Sect. 3.1), compute accretion luminosities for each object in a self consistent manner (Sect. 3.2), and describe in detail how we calculate [Ne II] and H I fluxes taking into account any possible contamination from water lines (Sects. 3.3 and 3.4). The last two sections (Sects. 3.5 and 3.6) discuss detections and correlations between line fluxes and adjacent continuum emission.

3.1. *Subsample of H I and [Ne II] sources: star and disk properties*

The properties of the 114 objects are summarized in Table A1. For each object we provide the stellar association it belongs to, the distance, spectral type (SpTy), visual extinction (A_V) as well as the effective temperature (T_{eff}) obtained using the T_{eff}-SpTy correlation of Kenyon & Hartmann (1995) and Luhman et al. (2003). Hα equivalent widths and stellar luminosities (L_{star}) have been collected from the literature using the references reported in Table A1, while the mass (M_{star}), and radius (R_{star}) were derived from the HR diagram and the Siess et al. (2000) evolutionary tracks.

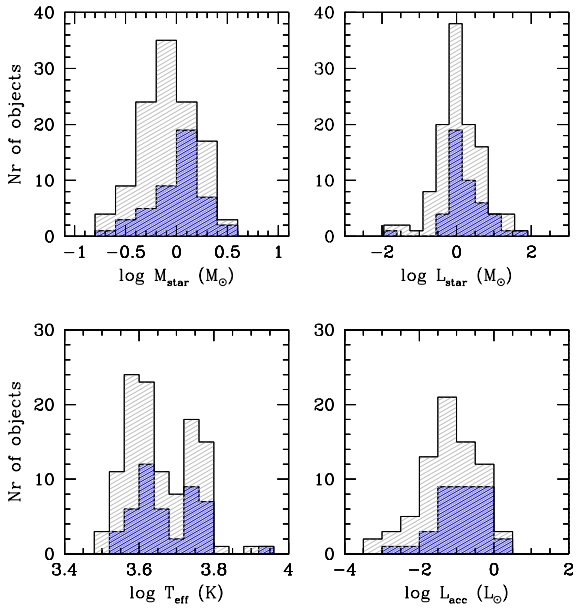

FIG. 2.— Distribution of mass, luminosity, effective temperature and accretion luminosity for all the objects in our sample (gray), and only the objects where H I(7-6) line has been detected (blue).

For multiple star systems the name we report in Table A1 is that of the primary star, which is the one with the earliest spectral type. However, in the table caption we list the separation of any other stellar companion within 10″ of the primary star. Given that the IRS/SH slit width is 4.7″, there are 15 objects with companions closer than 2.5″ that can contaminate the extracted IRS spectra. However, McCabe et al. (2006) show that only in 25% of the binary systems the secondary flux becomes larger than the primary flux at wavelengths >2 μm. Based on this, we assign the Spitzer spectrum always to the primary star in the 15 unresolved multiple systems.

We emphasize that the sample collected is biased in several ways: i) the number of objects with sky observations and multiple on-source exposures (see Sect. 2), ii) we only consider objects where the continuum has been detected and the signal-to-noise ratio of continuum level is higher than 5. Hence, we do not attempt any statistical study based on this sample.

3.2. *Accretion Properties*

To test whether mid-IR H I lines trace the accretion shock region and/or the accretion flow, we compare H I line luminosities with stellar accretion luminosities (L_{acc}). One of the most direct methods to measure L_{acc} is through modeling of the UV excess continuum emission produced by the accretion shock (e.g. Gullbring et al. 1998). However, only 17 objects in our sample have such measurements (AA Tau, CS Cha, DE Tau, DK Tau, DN Tau, DM Tau, DR Tau, GM Aur, HN Tau, LkCa 15, RX 132207.2-693812, TW Hya, SZ Cha, Sz 27, LkHa 330, RX J1852.3-3700 and RX J1842.9-3532, see Ingleby et al. 2013 and Manara et al. 2014). To measure accretion luminosities in a consistent way for all the objects in our sample we will use the Hα line luminosity. Even if this method allows an homogeneous estimate of the accretion lu-

minosity, we stress that the hydrogen lines in general, and the Hα line in particular, have several contributing mechanisms: accretion, stellar winds, jets, chromosphere (e.g. Hartmann et al. 1990, Calvet & Hartmann 1992). While this line is known to be an imperfect tracer of accretion in young stars, Rigliaco et al. (2012), among others, have shown that L_{acc} obtained from the UV excess emission and via indirect methods (e.g., Hα line luminosity) agree to within an order of magnitude.

To measure the accretion luminosity we first compute the Hα luminosity from the Hα equivalent width, the *R*- and/or *I*-band magnitude, and the extinction (A_V) for each object (e.g., Hartigan et al. 1995). The data were dereddened using Mathis's reddening law for R_V =3.1 (Mathis 1990). Next, we convert the Hα luminosity into L_{acc} using the relationship found by Rigliaco et al. (2012). Although this method provides self-consistent values for L_{acc} we are aware that the not-simultaneous observation of Hα, photometry, and A_V might introduce additional uncertainties in our estimates of L_{acc}. In Sect. 4.2 we describe how we account for these sources of uncertainty.

3.3. *[Ne II] Line Fluxes and Luminosities*

Water is largely detected in protoplanetary disks (e.g., Pontoppidan et al. 2010, Riviere-Marichalar et al. 2012), and its emission can contaminate other emission lines, as shown in the following sections. This is not the case for the [Ne II] line, that is quite isolated from other H_2O transitions. For this water-isolated and spectrally unresolved gas line we compute the flux by fitting a Gaussian profile to the observed line. We define the continuum level around the line as the mean value obtained sampling a 0.1μm wide region shortward and longward of the transition, and the uncertainty on the measured flux is the rms in these regions. The line flux and the associated 1σ uncertainty are reported in Table A2 for each detection. In the same table we provide 3σ upper limits to the flux when [Ne II] lines are not detected. Line luminosities are then computed using the distances reported in Table A1.

We have compared the measured [Ne II] line fluxes (as reported in Table A2) with those reported by other authors using either different data reduction techniques (Pascucci et al. 2007, Lahuis et al. 2007, Espaillat et al. 2013), and/or including any possible unresolved contribution from other species (H_2O and OH, Carr & Najita 2011). We find that the measured line fluxes and upper limits are in agreement within the errors (see Fig. 3).

3.4. *H I Line Fluxes and Luminosities*

The method used to compute the [Ne II] line fluxes and luminosities could be in principle applied to the H I lines. However, because the H I(7-6) and H I(9-7) transitions are very close to water lines we must subtract any possible contamination from water before measuring line fluxes. We proceed as follows. In Sect. 3.4.1 we identify the objects that lack detectable water emission (hereafter, 'water-free' disks[2]) and the objects where water is detected in their spectra ('water-contaminated' disks). For the water-free disks we compute line fluxes as in Sect. 3.3. For the water-contaminated disks we discuss a procedure to subtract water emission from the H I lines (Sect. 3.4.2) and then we measure the residual H I fluxes after water subtraction.

[2] We note that these objects might possibly show water contribution in higher S/N or higher resolution spectra.

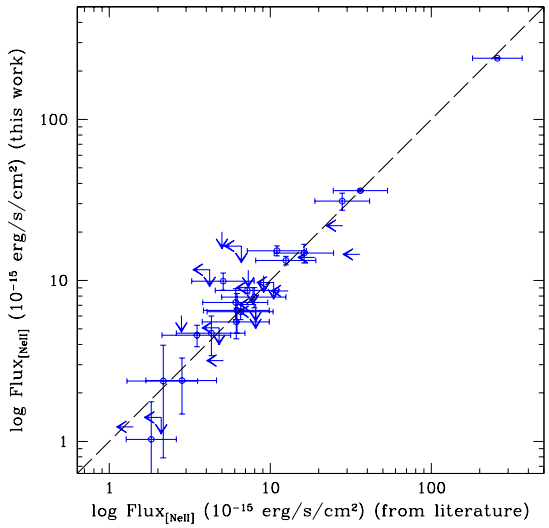

FIG. 3.— Comparison between the [Ne II] line fluxes measured following the data reduction chain explained in Sect. 2 and the line fluxes obtained from the literature using different data reduction techniques.

3.4.1. *Water-contaminated vs water-free disks*

To search for water emission in the source spectra we used the two water line complexes at 15.17μm and 17.22μm identified by Pontoppidan et al. (2010). These lines were selected because they are strong and more isolated than most other H_2O lines. Following Pontoppidan et al. (2010), we define as water contaminated those spectra in which both the H_2O lines are detected above 3σ. We do not find any case where one of the two lines is detected above 3σ, and the other one is not detected.

Among the 114 disks in our sample, 33 are water-contaminated. The remaining objects have water-free spectra. We show in Figure 4 a water-contaminated spectrum (DR Tau), and a water-free spectrum (DE Tau) in the region around the 15.17μm and 17.22μm water lines. For comparison we also show a synthetic water spectrum modeled assuming a gas temperature of 600 K and a water column density of 10^{18} cm^{-2} (see next Section). Line fluxes, together with the uncertainties and continuum level next to the lines are reported in Table A2.

3.4.2. *Correcting for water emission*

Water emission lines have been detected towards many protoplanetary disks using the *Spitzer*/IRS spectrograph (Pontoppidan et al. 2014 for a review). Previous studies have shown that a simple model, which assumes a plane-parallel slab geometry and gas in local thermal equilibrium (LTE), can reproduce relatively well the fluxes of the observed H_2O lines (e.g., Carr & Najita 2011). However, we are aware that these assumptions ignore the non-LTE effects and the complex geometric structure of disks (see Meijerink et al. 2009). We use this simple model as developed in Pascucci et al. (2013) to subtract any water contamination from the H I lines. The specific LTE model takes the molecular parameters from the HITRAN 2008 database (Rothman et al. 2009) and requires only 4 inputs: the gas temperature, the water column density, the radius of the emitting area, and the line width (which we

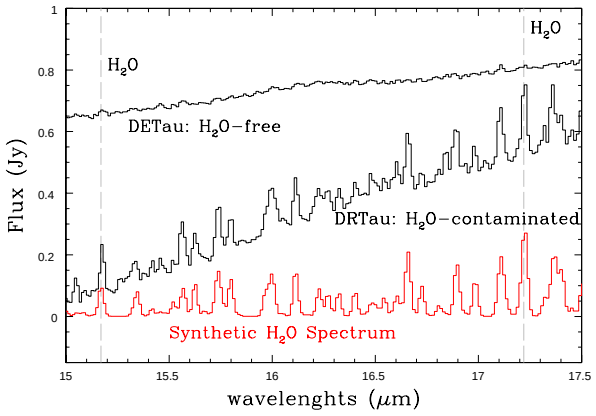

FIG. 4.— Examples of water contaminated (DR Tau), water-free (DE Tau) and synthetic H_2O spectrum in the wavelength region around the two isolated H_2O lines at 15.17 and 17.22 μm. The target spectra are shown in black, and the synthetic water spectrum is shown in red.

assume to be the thermal line width, i.e., variable with temperature). We created a grid of synthetic spectra using five different gas temperatures (T=[400, 500, 600, 700, 800]) and water column densities (N_{col}=[10^{17}, 5×10^{17}, 10^{18}, 5×10^{18}, 10^{19} cm^{-2}]) and assumed the same projected emitting area of radius 1 AU. The chosen inputs span the range of parameters inferred for the warm disk atmosphere of T Tauri stars (Carr & Najita 2011, Salyk et al. 2011).

The water lines contaminating the hydrogen lines are centered at $\sim$12.39μm and $\sim$11.31μm for the H I(7-6) and H I(9-7) transition, respectively. In the following we will refer to these lines as "H_2O-contaminating". To subtract off the water contribution to the observed H I lines we have searched the synthetic spectra for *isolated* H_2O lines with similar properties as the H_2O-contaminating ones. The two water lines that we have identified will be called in the following "H_2O-isolated" lines and have the following characteristics: they have similar lower energies (E_{low}) and Einstein A-coefficients (A_{ul}) (within 15% at most) as the H_2O-contaminating lines; H_2O-isolated line is within 1μm from the corresponding contaminating line, so that the continuum level does not substantially change. Following these criteria we find that the H_2O-isolated line at 13.13μm is the best match for the H_2O-contaminating line at 12.39μm, while the H_2O-isolated at 11.96μm has very similar properties as the H_2O-contaminating at 11.31μm (see Table 2). We show in Fig. 5 the ratio between the H_2O contaminating/isolated line fluxes for all the temperature and column density of the synthetic spectra. The ratios are quite constant among all the synthetic spectra, with $H_2O(12.39\mu m)/H_2O(13.13\mu m)\sim3.5$ and $H_2O(11.32\mu m)/H_2O(11.97\mu m)\sim1.0$, and vary within a factor 1.5 at most over our grid of synthetic spectra.

Once we identified the best water proxies, we searched all the spectra for H_2O-isolated lines. In the SH-*Spitzer*/IRS spectra none of the 83 water-free spectra shows these lines, as expected because the H_2O lines become weaker at shorter wavelengths (e.g., Salyk et al. 2011). In the 33 water-contaminated disks, we subtracted the water contribution from the H I line fluxes as follows: if the H_2O-isolated line is detected above the 3σ level, we use it and its ratio to the nearby H_2O-isolated line to compute the H_2O-contaminating flux (as $H_2O(12.39\mu m)=3.5\times H_2O(13.13\mu m)$ and $H_2O(11.32\mu m)=H_2O(11.97\mu m)$, respectively for H I(7-6) and H I(9-7)), and then subtract it from the measured HI line flux. If the H_2O-isolated is not detected, we subtract its 3σ upper limit from the observed H I flux. After subtracting the water contamination from the observed line flux, we obtain the actual hydrogen line flux. The final line fluxes after water subtraction and errors are reported in Table A2. We also show in parenthesis the total flux observed before subtracting the water contribution in the objects where the H I lines are detected. In the case of H I non-detections we provide the 3σ upper limit to the flux. Any other water contribution, if present, is within the 10% absolute flux uncertainty. As for the [Ne II], we have compared our H I(7-6) line flux measurements with the few already reported in the literature (Pascucci et al. 2007, Carr & Najita 2011). We find that the reported values are in agreement within the errors and the absolute flux uncertainty.

TABLE 2
H_2O LINE PROPERTIES

Line	Wavelength (μm)	A_{ul} (s^{-1})	E_{low} (cm^{-1})
H_2O-contaminating	11.3241	1.576	2746.02
H_2O-contaminating	12.3962	7.665	3211.21
H_2O-isolated	11.9681	1.281	2629.33
H_2O-isolated	13.1325	6.788	3244.60

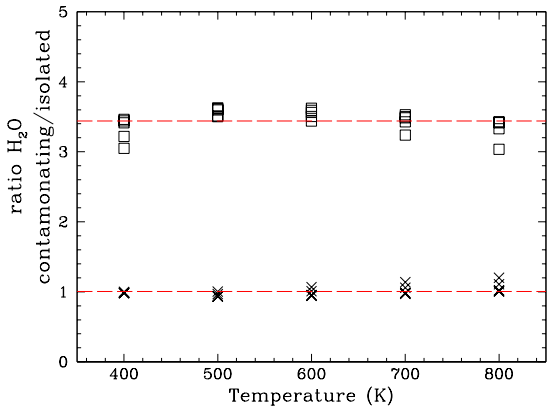

FIG. 5.— H_2O contaminating/isolated line ratios: crosses for $H_2O(11.32\mu m)/H_2O(11.97\mu m)$ and squares for $H_2O(12.39\mu m)/H_2O(13.13\mu m)$. The ratios are computed for all the temperatures and column densities explored with the model grid. At each temperature there are 5 ratios, one for each value of the column density.

3.5. *Line Detections Summary*

We detect the [Ne II] line at 12.81 μm in 49 objects in our sample. Among the 67 objects where the [Ne II] line is not detected, 37 are full disks, 4 are transitional disks and 26 are debris disks. One debris disk has a [Ne II] line detection (Rigliaco et al. in preparation). After correcting for water contamination, we identify 46 objects with an H I(7-6) detection above 3σ, 11 of them also show the weaker H I(9-7) line. In 6 spectra we detect all three lines of interest: the [Ne II], the H I(7-6), and the H I(9-7) line. Line detections are summa-

TABLE 3
LINE DETECTIONS

Detected Lines	Total number of objects	Relative % F	T	D
[Ne II]	49	67	31	2
H I(7-6)	46	57	26	17
H I(9-7)	11	55	27	18
[Ne II]+H I(7-6)	24	50	46	4
H I(7-6)+H I(9-7)	11	55	27	18
[Ne II]+H I(7-6)+H I(9-7)	6	50	50	0

NOTE. — The second column shows the total number of objects where the lines listed in Column 1 have been detected. The 3rd, 4th and 5th columns report the relative percent of these objects in full, transitional and debris disks respectively.

rized in Table 3. We note that all objects where water emission is detected are full disks and none of the transitional or debris disk spectra have detectable water emission. Thus, expanding upon previous results (e.g., Pontoppidan et al. 2010), our analysis shows that the absence of water lines in the SH module is typical to more evolved transitional and debris disks, while full disks can either have a water rich spectrum or not.

Interestingly, we detect H I(7-6) in 8 young (<20 Myrs) debris disks. We will discuss these objects in Sect. 4.5.

3.6. *H I lines versus continuum luminosity*

Once we accounted for the water contribution and measured the H I(7-6) and H I(9-7) line luminosities, we investigated their behavior as a function of the continuum luminosity around the lines (Fig. 6). As also seen in other IR lines ($H_2S(2)$, [Fe I] at 24μm, [Ne II], e.g., Lahuis et al. 2007), there is a correlation between the H I mid-IR lines and the continuum flux level next to the lines. This correlation could be influenced, but it is not exclusively driven, by the more favorable contrast between line and continuum luminosities where the continuum is lower (as demonstrated by finding the same increasing trend between the line to continuum vs continuum flux). We have also investigated this correlation for different disk morphologies and find that debris disks have lower H I line luminosities and continuum luminosities than transitional and full disks. In order to understand whether these differences are statistically significant we have measured the mean and standard deviation of line and continuum luminosities for the three different disk morphologies (shown as solid lines in Fig. 6). From this analysis we conclude that, even if transitional disks appear having lower H I and continuum luminosities than full disks, their difference is within 1σ uncertainty, and thus not statistically significant. On the other hand, debris disks show consistently lower luminosities, both in the continuum and in the lines.

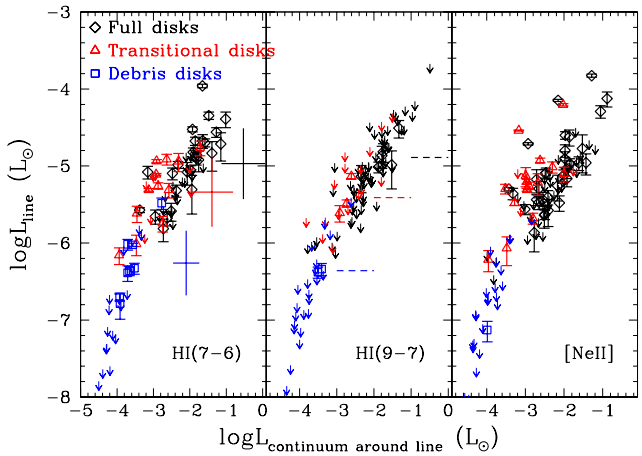

FIG. 6.— H I(7-6), H I(9-7) and [Ne II] line luminosity versus continuum luminosity around the lines. Black-diamonds represent objects surrounded by a full disk, red-triangles are for transitional disks, blue-squares for debris disks. Downward pointing arrows are upper limits. In the left panel solid lines represent the mean value of line and continuum luminosities with the 1σ uncertainty for the objects where both line and continuum are detected. In all cases, the mean value for the x-axis has been shifted by +1.5 for clarity. In the middle panel we show the mean in the line luminosity as dashed lines, given the large fraction of non-detections. We note again that the measure of the means is only based on the detections, and for the H I(9-7) lines the upper limits are more numerous than the detections.

4. DISCUSSION

4.1. *Mid-IR H I lines: disk tracers?*

In the following we compare the [Ne II] line fluxes obtained from our reduction of the *Spitzer* spectra with those of the H I lines to test if these two lines could trace the same region in/around the disk. In particular, we will test if [Ne II] and H I lines may trace the disk surface. As mentioned in Sect. 1, [Ne II] lines have been studied both with *Spitzer* and with ground-based spectrographs at higher spectral resolution. These studies have shown that the [Ne II] line mostly traces jets/outflows in high-accreting stars and the hot disk surface in lower accretors ($\dot{M}_{acc} \lesssim 5 \times 10^{-8} M_\odot$/yr, e.g. Güdel et al. 2010, Sacco et al. 2012). Unfortunately, similar ground-based followup studies have not yet been carried out for the mid-IR H I lines, hence a direct comparison of high-resolution spectra cannot be done. The vast majority of the objects in our sample (namely, 85%) for which we have computed L_{acc} (and $\dot{M}_{acc}$) can be classified as "low-accretors" according to the threshold value reported above (Güdel et al. 2010). Hence, for most of our sources a detection of [Ne II] in the *Spitzer* spectrum is most likely due to emission from the hot disk surface.

The left panel of Figure 7 shows a log-log plot of the H I(7-6) line luminosity at 12.37μm versus the [Ne II] line luminosity at 12.81μm . The luminosities of the two lines, when they are both detected, appear positively correlated, with *Pearson* correlation coefficient of ∼0.9, and p-value∼10^{-6}. The correlation becomes weaker when upper limits are considered. However, this correlation could be affected by the underlying correlation between the line luminosities and the continuum luminosities around the line (see Figure 6 and discussion in Sect 3.6). To account for this possible effect we plot in Fig. 7 (right panel) the equivalent widths of the two observed lines. The [Ne II] and H I(7-6) equivalent widths do not show any obvious correlation, and the *Pearson* correlation coefficient drops to ∼0.4 (weak correlation) and p-value∼0.04. This result suggests that the positive relation between the H I(7-6) and [Ne II] line luminosity is caused by the correlation between the line and nearby continuum.

To further test this finding, we compare the observed H I line luminosities with those predicted by models of disks irradiated by high-energy photons (Ercolano et al. 2008, Hollenbach & Gorti 2009, Ercolano & Owen 2010). In an EUV (13.6 eV< $h\nu$ <0.1 keV) irradiated disk the predicted $L_{HI(7-6)}/L_{[NeII]}$ ratios are as small as ∼0.008 (Hollenbach & Gorti

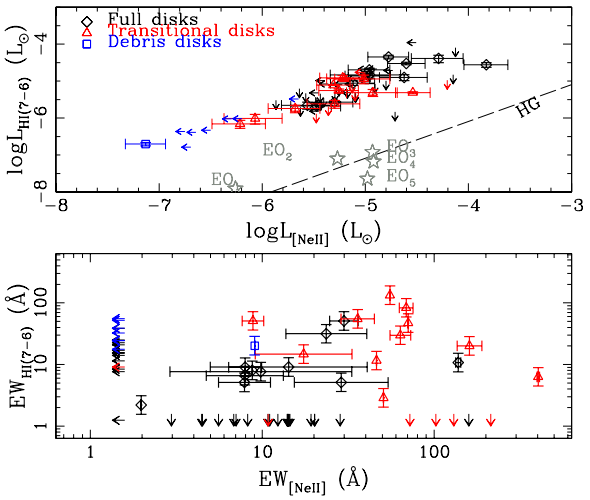

FIG. 7.— Top: H I(7-6) versus [Ne II] line luminosity. We also show the prediction of these line luminosities for different theoretical models. The black-dashed line (labeled as HG) shows the H I(7-6)/[Ne II] line relation for a disk irradiated by EUV photons (Hollenbach & Gorti 2009). The gray stars refer to X-ray irradiated primordial disk with $\log L_X$=29.3 (EO_1), $\log L_X$=30.3 (EO_2), and transitional disks illuminated by $\log L_X$=30.3 erg/s with inner hole 8.3 AU (EO_3), 14.2 AU (EO_4) and 30.5 AU (EO_5), as measured by Ercolano & Owen (2010). Bottom: comparison between the equivalent widths of the two lines.

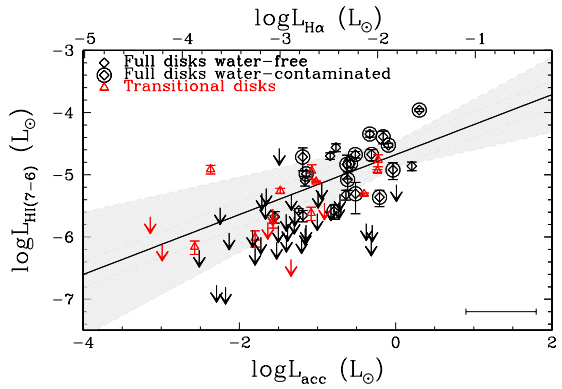

FIG. 8.— H I(7-6) line luminosity versus Hα line luminosity and L_{acc}. Circles are drawn around water-contaminated objects. The black-solid line shows the best linear regression line and the shaded-gray area represents the approximate 95% confidence intervals (2σ) on the regression line. The typical error is shown in the bottom-right corner.

2009) because the radiative recombination rate of hydrogen is smaller than the electronic collisional excitation rate of [Ne II]. The observed line ratios are instead almost two orders of magnitude higher than the predicted ones (see Table A2). A disk irradiated also by X-rays ($h\nu$ >0.1keV) still produces an H I(7-6) line luminosity more than one order of magnitude smaller than the ones observed (Ercolano et al. 2008, Ercolano & Owen 2010). The comparison between the observed line luminosity and different theoretical models shows that it is unlikely that the observed HI(7-6) lines trace the same hot disk atmosphere that produces the [Ne II] lines.

In summary, both the lack of correlation between the [Ne II] and the H I(7-6) equivalent widths, and the comparison with model predictions suggest that the H I(7-6) line is not tracing the same disk region as the [Ne II] line, and that the H I lines are unlikely disk gas tracers.

4.2. *Mid-IR H I lines: accretion indicators?*

Hydrogen recombination lines from the Balmer to the Paschen and Brackett series (in the UV, optical and near-IR wavelengths) have been extensively studied over the years, and have been convincingly found to trace infalling material onto the star, as demonstrated by their broad line profiles consistent with gas at almost free-fall velocity onto the star (e.g., Alcalá et al. 2014). Nevertheless, these line profiles are also known to have other contributing mechanisms: stellar wind, jet, chromosphere. Recently, Salyk et al. (2013), using high-resolution spectroscopy extended the accretion tracers to the Pfund series lines, including the Pfβ hydrogen recombination line at 4.65μm (H I(7-5)).

To test if the H I mid-IR lines can be used as accretion indicators, in the rest of this section we focus on the subsample of full and transitional disks for which an estimate of the Hα equivalent width is available in the literature (see Table A1). We chose to use the H I(7-6) line (the strongest among the H I lines observed with the *Spitzer* SH module) to maximize the number of detected sources. Among the objects considered in this work, 73 have an estimate of the accretion luminosity from the Hα line (34 of those have an H I(7-6) detection).

We show in Fig. 8 the H I(7-6) line luminosity as a function of the Hα line luminosity and the accretion luminosity measured as described in Sect. 3.2. There is a linear correlation between $\log L_{HI(7-6)}$–$\log L_{acc}$. To estimate the best fit regression line for the objects with detection in both quantities, and to account for the measured errors in both the x- and y-axes we employe the Bayesian method as implemented in the IDL routine *linmix_err* (Kelly 2007). The error on the y-axes is driven by the uncertainty on the observed line fluxes. The uncertainty in our estimate of L_{acc} is given by the combination of several factors: the uncertainty on the Hα equivalent width, the non-simultaneous observation of Hα, photometry, and extinction, the error on the extinction value (A_V) and the errors on slope and intercept of the L_{acc}-$L_{H\alpha}$ relationship. Following Costigan et al. (2012) we assume a mean amplitude of variation in the derived accretion luminosities of ∼0.37 dex, which includes Hα equivalent width uncertainties, time variability, and the error in the L_{acc}-$L_{H\alpha}$ relationship. We also consider an uncertainty on A_V of 1 mag (e.g. Edwards et al. 2013), which gives a final uncertainty on L_{acc} ∼0.5 dex. We find the following best fit regression line between the H I(7-6) line luminosity and the accretion luminosity:

$$logL_{HI(7-6)}/L_\odot = (0.48 \pm 0.09) \times logL_{acc}/L_\odot - (4.68 \pm 0.10) \quad (1)$$

We have checked that the $\log L_{HI(7-6)}$–$\log L_{acc}$ correlation is not driven by the distance and/or stellar luminosity dependence. We have also ascertained that the relationship between the luminosity of the H I(7-6) line and L_{acc} measured through UV-excess emission for only 15 objects (see Sect. 3.2) lies within the 95% confidence intervals. We note that the uncertainty on the intercept we find in Eq. (1) is similar to the those found using different H I lines (e.g., Alcalà et al. 2014), suggesting that the scatter around the fit is similar when using different H I lines. On the other hand, the slope found in Eq. (1) is shallower than the ones found for the H I lines in the optical and near-IR wavelengths. This suggests that the MIR lines are less sensitive to accretion luminosity variations.

Knowing L_{acc} and the stellar properties we can also compute the mass accretion rate ($\dot{M}_{acc}$) using the classical relation

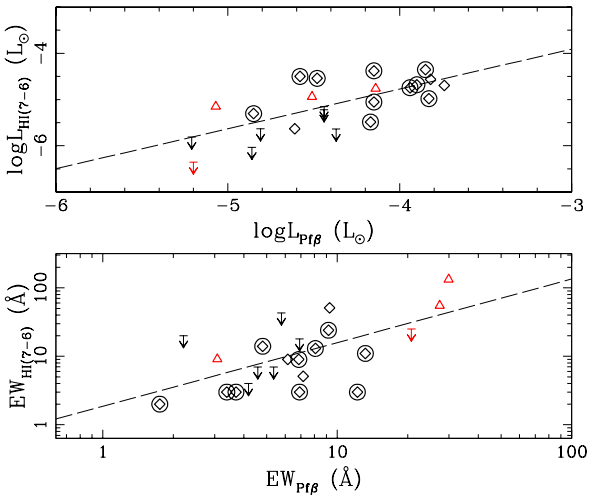

FIG. 9.— Top: H I(7-6) versus Pfβ line luminosity. The black-dashed line hows the least square fit. Bottom: comparison between the equivalent widths of the two lines.

from Gullbring et al. (1998):

$$\dot{M}_{acc} = \left(1 - \frac{R_{star}}{R_{in}}\right)^{-1} \frac{L_{acc} R_{star}}{G M_{star}} \quad (2)$$

where R_{in} is the radius at which the accreting gaseous disk is truncated due to the stellar magnetosphere. In full disks, R_{in} has been found ranging between $3R_{star}$ and $10R_{star}$ (Johns-Krull 2007), and usually R_{in}=$5R_{star}$ is assumed. In our sample we do not only consider full disks, but also transitional disks where the geometry of the gas disk around the star could be different. We do not speculate on how that could change for more evolved disks, and we will use the R_{in}=$5R_{star}$ for all the different disk morphologies.

For the subsample of objects where the Pfβ line is detected (Salyk et al. 2013) and the H I(7-6) is detected and not water contaminated (this work) we find that their luminosities, as well as equivalent widths, are correlated with *Pearson* correlation coefficients ∼0.7 and ∼0.8, respectively, and p-value ∼0.007 and ∼0.05, respectively (Fig. 9). While Salyk et al. 2013 report lower Pfβ luminosities and high EWs for 5 transitional disks with respect to full disks, we do not find any statistically significant difference in the H I(7-6) lines in our much larger samples of transitional and full disks (see also Sect. 4.1). We also note that these two samples have not statistically different L_{acc}, as also reported in other studies where $L_{acc}$are consistently derived (Keane et al. 2014, Fang et al. 2009).

The fact that the H I(7-6) line correlates both with the Hα and Pfβ lines suggests that the Humphreys α line at 12.37μm is likely an accretion indicator, as the hydrogen lines belonging to other series (Hα (e.g., Muzerolle et al. 1998, Paβ (e.g., Folha & Emerson 2001), Brγ (e.g., Natta et al. 2006), Pfβ (Salyk et al. 2013)).

Speculating on the correlation reported in Eq. (1), we can measure what the mass accretion rates would be if the H I(7-6) lines in the debris disks spectra were accretion related. We find that debris disks with detected H I lines span the lower range of mass accretion rate (covering the range between $\times10^{-10}$–2×10^{-12} M$_\odot$/yr), as would be expected by their more evolved stage and the lack of gas in their disks.

4.3. *HI Line Ratios*

Hydrogen line ratios can be used as a diagnostic tool to constrain the physical conditions (density and temperature) of the emitting gas. Among the sample of objects analyzed in this paper, in 46 the H I(7-6) transition is detected above 3σ, and 11 of those show as well a detection of the H I(9-7) transition. The detected H I(9-7)/H I(7-6) line ratios range between ∼0.4 and ∼1.1. The upper limits cover a similar range. We can retrieve information on the physical properties of the emitting gas by comparing the observed ratios with those predicted by two different models: the Case B (Hummer & Storey 1987, Storey & Hummer 1995) and the Kwan and Fischer (Kwan & Fischer 2011, KF) models. In these models the H I line ratios ranges between ∼0.3–0.5 in the optically thin regime, and become higher (between ∼1.0–2.0) when the lines are optically thick.

4.3.1. *Case B models*

The Case B model for radiative ionization and recombination (Baker & Menzel 1938) assumes that gas is optically thick to Lyman series photons and optically thin to photons associated to all other transitions. This model has been largely used to retrieve the properties of gas accreting onto T Tauri stars. However, results found considering individual objects and different hydrogen lines indicate very different physical properties of the accreting gas (Bary et al. 2008, Rigliaco et al. 2009, and Edwards et al. 2013 for a review). Using the interactive online server[3] (Hummer & Storey 1987, Storey & Hummer 1995), we computed the predicted line ratios for a range of temperatures from 1000 K to 15,000 K and electron densities from 10^9–10^{12}cm^{-3} (see Fig. 10).

The predicted H I(9-7)/H I(7-6) line ratios are almost constant (between ∼0.3-0.4) for T≥5000 K over the electron density range considered here. As the temperature decreases under 5000 K, the predicted ratio increases from ∼0.3 to ∼0.7 until electron densities $n_e \lesssim 10^{10}$cm^{-3}, and then decreases to ∼0.2 when n_e becomes larger. Thus, a large range of temperatures, down to T∼1000 K, is required to explain most of the observed ratios. Still, ratios as high as 1.0 cannot be explained by the Case B models. In addition, as pointed out in Edwards et al. (2013), the necessity to maintain low line optical depths in the Case B models puts some restrictions to the applicability of this model to regions with high densities such as accretion funnels in YSOs.

4.3.2. *Kwan & Fischer models*

Kwan & Fischer (2011) predicted hydrogen line ratios using a different approach than the Case B, in that they consider individual line optical depths. The inputs of these calculations are the gas temperature, the hydrogen density, the ionization rate (which was not specified in the case B models) and the velocity gradient with respect to the emission length scale (see Kwan & Fischer 2011 and Edwards et al. 2013 for more details). These parameters are chosen to replicate conditions in the region of winds and accretion flows in accreting YSOs.

We show in Figure 11 the comparison between the KF model predictions for the H I(9-7)/H I(7-6) line ratio and the observations[4]. The input gas temperatures span from 5000 K to 15,000 K, and given that the $(n_e)/(n_H)$ ratio is between 0.1 and 1.0, the hydrogen densities (n_H) cover similar electron densities as those shown in Fig. 10 for the Case B models.

[3] http://cdsarc.u-strasbg.fr/viz-bin/Cat?VI/64

[4] Hydrogen line ratios for the Kwan & Fischer models are publicly available: http://iopscience.iop.org/0004-637X/778/2/148/suppdata/data.tar.gz

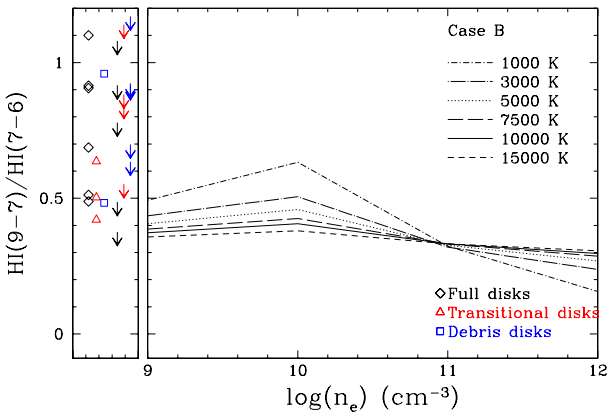

FIG. 10.— HI(9-7)/HI(7-6) line ratio versus the electron density. Case B models for different temperatures as labeled. The range of the observed ratios is shown along the left side, where the typical uncertainties on the observed ratios are also plotted.

The ratios suggested by the KF models are almost constant for all the temperatures until $n_H \sim 10^{10}$ cm^{-3}. As the density increases, the line optical depth increases as well, first for the (7-6) transition, which explains the steep increase in line ratio. For $(n_H) > 10^{11}$cm^{-3} both lines have large optical depths which explains the plateau. While the general behavior is similar for all temperatures, the specific transition density is $\sim 10^{10}$ cm^{-3} for T$\gtrsim$10,000 K and $\sim 5 \times 10^{10}$cm^{-3} for lower temperatures. Thus, unlike the Case B models, the KF models can explain all the observed line ratios with a limited range of temperatures (5000 – 15,000 K) and relatively narrow range of gas densities ($n_H \sim 10^{10} - 10^{11}$cm^{-3}).

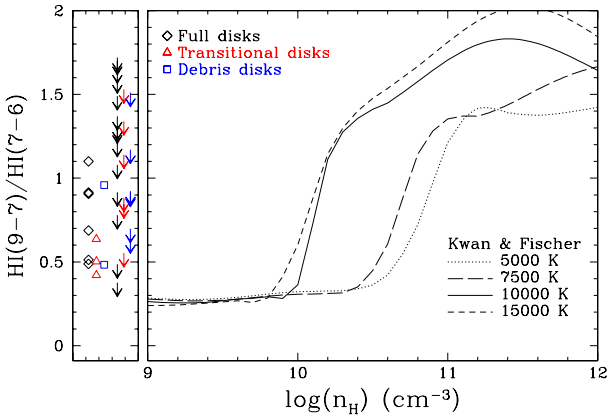

FIG. 11.— HI(9-7)/HI(7-6) line ratios versus the hydrogen column density for the observed ratios. Kwan & Fischer models for different temperatures as labeled. Symbols as in Fig. 10

4.3.3. *Comparison between model predictions and gas physical properties*

According to Martin (1996), who modeled the temperature and density profiles for gas channeled in magnetospheric accretion funnels, the typical temperatures in these regions are ∼6000 K, and hydrogen densities are as high as 10^9–10^{10}cm^{-3}. Muzerolle et al. (2001), considering the Hα and Hβ lines, found that the temperature of magnetospherically accreting gas ranges between 6000 K – 12000 K for a range of accretion rates between 10^{-6} – 10^{-10} M$_\odot$/yr. Recently, Edwards et al. (2013) examined near-IR hydrogen line ratios for a sample of T Tauri stars. They find that the hydrogen density (n_H) in the line formation region is constrained within 2×10^{10}–2×10^{11}cm^{-3}, while the temperature is not well delineated.

If the hydrogen mid-IR lines are tracing accretion at least in full and transitional disks, the observed H I(9-7)/H I(7-6) line ratios cannot be explained by the gas properties predicted by the case B models. In fact, as we have seen is Sect. 4.3.1 and Fig. 10 the observed line ratios require gas colder than 5000 K irrespective of the electron densities. Such physical properties, and in particular such low temperatures, are unlikely in the magnetospheric accretion columns, in which we expect temperature of at least a factor of two higher and a much narrower range in density (e.g., Muzerolle et al. 2001).

On the other hand, the KF models suggest gas properties that better match the scenario in which the mid-IR hydrogen lines are produced in the accretion funnels because they predict an hydrogen column density (n_H) between $10^{10} - 10^{11}$ cm^{-3}, and a temperature range between 5,000 and 15,000 K (see Fig. 11). The analysis of the H I(7-6)/Pfβ line ratios for the subsample of objects where these two lines have been observed adds additional constraints. In all but one object the observed line ratio is consistent with the KF model predictions for n_H between $\sim 10^{10}$– $\sim 10^{11}$ cm^{-3} and T>5,000 K (see fig. 12). These results not only suggest that in most cases H I(7-6) and Pfβ might have a common origin, but that this origin is from hot gas with relatively high hydrogen column density (as expected in the accretion funnels). The objects where both H I(7-6) and Pfβ are detected, but the H I(7-6)/Pfβ line ratio does not fit the Kwan & Fischer models are VW Cha and TW Hya, where the H I(7-6)/Pfβ line ratios is ∼0.9.

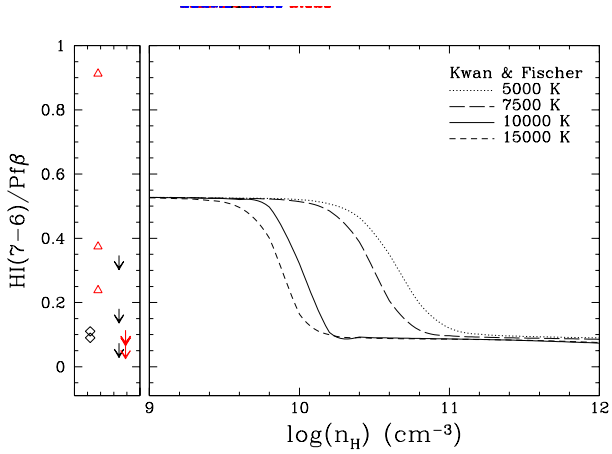

FIG. 12.— HI(7-6)/Pfβ line ratios versus the hydrogen column density. Kwan & Fischer models for different temperatures as labeled. Same symbols as Fig. 10.

We note that similarly stringent constraints on the gas physical properties cannot be placed when using shorter wave-

lengths hydrogen lines. In particular, we have analyzed model predictions (both case B and KF models) for the H I(7-6)/Hα and H I(7-6)/Paβ lines. We find that the observed ratios span a wider range of values, making the comparison with models inconclusive. This could be due to the different optical depths of the compared lines, which could affect the Hα line as well as other short wavelength transitions, or to time variability, which may be more pronounced at shorter wavelengths. In the case of the H I(7-6)/Hα line ratio we must also take into account that Balmer series lines in general, and Hα line in particular, have quite complicated profiles, with a variety of structures that include blueshifted absorption and line asymmetries (e.g., Basri & Batalha 1990).

4.4. *Chromosphere and High-Density Wind*

The analysis carried out so far has shown that the H I mid-IR lines are very unlikely disk tracers. Moreover, the correlation between the H I(7-6) line and the accretion luminosity, and the H I line ratios support an origin of these lines in the accretion funnels for full and transitional disks. However, Hollenbach & Gorti (2009) discussed two other possibilities for the origin of H I mid-IR lines: an internal wind shock with high speed ($v_s \gtrsim 100$ km/s) and close to the wind origin ($\lesssim$1 AU), or the stellar chromosphere (see also Pascucci et al. 2007).

An internal shock origin, even if plausible for full disks, would be very difficult to reconcile with the detection of H I in the spectra of transitional and debris disks. Transition disks rarely show signs of outflows activity (see for example the optical forbidden line profiles in Hartigan et al. 1995), and debris disks have already dispersed most of their gas disk mass (e.g. Pascucci et al. 2006). While it is possible that mid-IR hydrogen lines trace different environments depending on the stellar/disk evolutionary stage, as shown for the [Ne II] line (see Sect. 1), a wind shock origin cannot explain the detections in transitional and debris disks.

The mean chromospheric electron density in T Tauri stars is $n_e \sim 10^{11}$cm^{-3} (Giampapa et al. 1981, or $10^{11} \lesssim n_H \lesssim 10^{12}$cm^{-3} if $0.1<(n_e)/(n_H)<1$, see Sect. 4.3.2). According to the KF model at these high densities the H I(7-6) and (9-7) transitions would be both optically thick, hence line ratios should be $\gtrsim$1. Only few sources in our sample sport such large line ratios. Another way that we have employed to investigate the chromospheric origin of the H I lines is to consider the effect of the chromospheric emission on the measured accretion luminosity. Manara et al. (2013), quantified this effect by analyzing a sample of high dispersion spectra of non-accreting low-mass T Tauri stars. Measuring the Hα emission in non-accreting stars, and converting this value into an accretion luminosity, they find that the chromospheric activity can significantly contribute to the measured accretion luminosity when the latter is smaller that 10^{-3}L$_\odot$, and that this contribution is strongly dependent on the object's effective temperature (hence spectral type). They derive a correlation between T$_{\rm eff}$ and L$_{acc,noise}$ (the latter representing the chromospheric contribution to the accretion luminosity). Unfortunately, their sample is limited to objects with spectral type in the range K7-M9.5, and none of our debris disks falls in this range. In the following we will focus on the 42 objects with T$_{\rm eff}$ <4100 K and with an estimate of L_{acc} (see Table A1). In Fig. 13 we plot L$_{acc,noise}$ obtained using the correlation provided by Manara et al. (2013, their Eq. 2) versus L_{acc} as reported in Table A1. 13 of these objects also shown a detection in the H I(7-6) line (green-filled symbols). There is a small number of targets, where the ratio is not more than 5, for which the chromospheric contribution could substantially influence the estimate of the accretion luminosity. However, in the majority of objects L_{acc} is at least 5 times bigger than its chromospheric contribution, meaning that the latter is well within the estimated uncertainty on L_{acc}. Moreover, the objects where the H I(7-6) line is detected (identified as green-filled symbols in Fig. 13) span all over the range of L_{acc}.

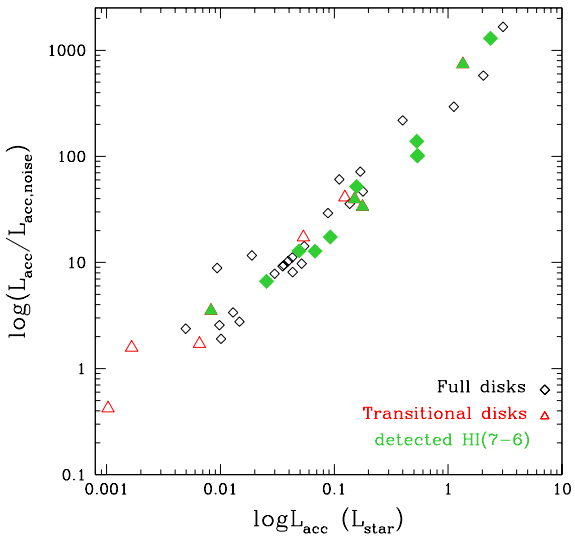

FIG. 13.— Contribution to the accretion luminosity from chromospheric emission (L_{acc}/L$_{acc,noise}$), measured using the relation found by Manara et al. (2013), versus L_{acc} for all the objects with T$_{\rm eff}$ <4100 K. Symbols are as labeled. Filled symbols refer to objects where H I(7-6) is detected.

We can only test the chromospheric contribution over the accretion luminosity for ∼40% of the total sample, where T$_{\rm eff}$ <4100 K. For this subsample the previous analysis suggests that the H I lines are not contaminated by the chromospheric contribution at a significant level. We could not extend this analysis to objects with higher temperatures (earlier spectral types) and to debris disks. *It is possible that the H I mid-IR lines are tracing accretion in less evolved objects, while their contribution is only chromospheric in later evolutionary stages.*

The way to discriminate between accretion funnels, chromosphere and high-density wind is through ground-based high-resolution (10-20 km/s) spectroscopy. In fact, for H I lines originating in accreting gas we will observe broad lines (FWHM∼100 km/s, Muzerolle et al. 2001) close to the stellar velocity. A chromospheric component will be narrower (∼40 km/s) and centered at the stellar velocity (e.g. Herczeg et al. 2007). An internal shock origin will instead produce H I profiles that are as broad as 100 km/s and can be also blueshifted by the same amount.

4.5. *A closer look at the Debris Disks*

As already mentioned in the previous sections, this paper reports the first detection of H I(7-6) and H I(9-7) gas lines in debris disks (we also detect the [Ne II] gas line in the *Spitzer* spectrum of HD 35850, as will be discussed in Rigliaco et al., in preparation). We show in Fig. 14 a compilation of the 8

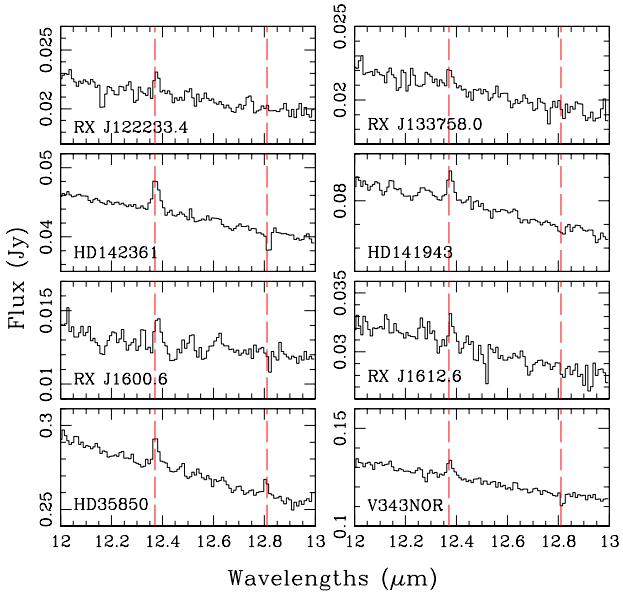

FIG. 14.— *Spitzer* spectra of the 8 Debris Disks where the H I(7-6) line is detected.

debris disks line profiles where the H I(7-6) line has been detected. In the following we will investigate the properties of all the debris disks we have re-reduced, either with detected H I(7-6) lines or not (as reported in Tables A1 and A2). All these debris disks are observed within the FEPS[5] *Spitzer* Survey (Meyer et al. 2006), and we collect the quantities plotted in Figure 15 and reported in Table 4 from the FEPS Database[6].

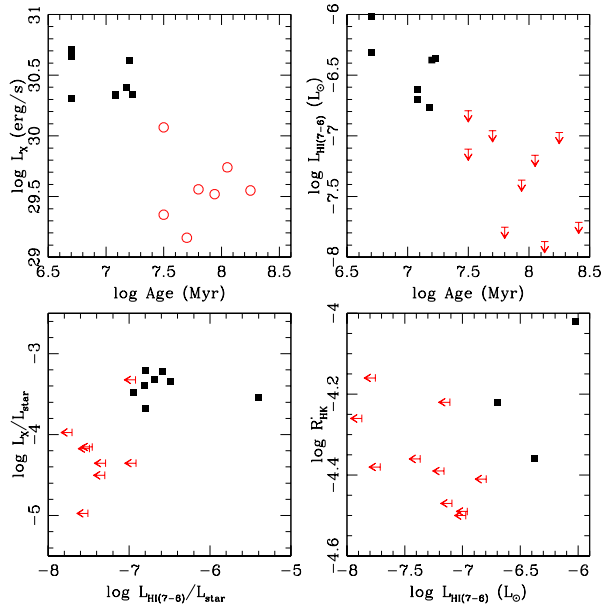

FIG. 15.— Top-left panel: X-ray luminosity versus Age. Black squares and red-open circles refer to objects with detected and not-detected H I(7-6) line, respectively. Top-right panel: L_X/L_{star} versus $L_{HI(7-6)}/L_{star}$. Bottom-left panel: chromospheric activity diagnostic $R^{'}_{HK}$ versus the H I line luminosity. Bottom-right panel: H I(7-6) line luminosity versus Age.

[5] Formation and Evolution of Planetary Systems
[6] http://feps.as.arizona.edu/index.html

TABLE 4
DEBRIS DISKS PROPERTIES

Name	Age (Myr)	log L_X (erg/s)	$R^{'}_{HK}$	Ref
1RXS J121236.4-552037	17	30.32	···	6,2
1RXS J122233.4-533347	17	30.34	···	6,2
1RXS J130153.7-530446	17	30.01	···	6,2
HD 119269	17	30.60	···	6,2
1RXS J133758.0-413448	15	30.40	···	6,2
1RXS J161458.0-275013	5	30.05	···	7,2
HD 142361	5	30.71	-4.02	7,2,51
RXJ1600.6-2159	5	30.31	···	7,2
RXJ1612.6-1859	5	30.65	···	7,2
HD 35850	12	30.34	-4.22	10,2,9
V343Nor	12	30.33	···	10,2
HD 19668	257	···	-4.38	2,9
HD 25457	112	29.74	-4.39	5,2,9
HD 37484	50	29.16	-4.49	2,2,51
HD 12039	63	29.56	-4.16	2,2,51
HD 202917	32	30.07	-4.22	2,2,9
HD 141943	16	30.62	-4.36	2,2,4
HD 377	87	29.52	-4.36	2,2,9
HD 17925	55	29.07	-4.31	2,2,1
HD 32297	···	···	···	
HD 61005	135	···	-4.26	2,4
HD 69830	1860	···	-4.95	9,9
HD 134319	186	···	-4.35	9,9
HD 216803	400	28.33	-4.27	2,2,4
AO Men	12	30.16	-3.75	10,2,3

REFERENCES. — (1) Baliunas et al. 1996; (2) FEPS Database; (3) Grey et al. 2006; (4) Henry et al. 1996; (5) Luhman et al. 2005; (6) Mamajek et al. 2002; (7) Preibisch et al. 2002; (8) White et al. 2007; (9) Wright et al. 2004; (10) Zuckerman et al. 2001;

We first investigate a chromospheric nature for the mid-IR hydrogen lines. As shown in Figure 15 (top-left panel), all the debris disks where the H I(7-6) line is detected are younger and with higher X-ray luminosity. The latter is a chromospheric indicator of magnetic activity (e.g. Feigelson et al. 2007), and its decay with age could let us conclude that the H I line in debris disks are chromospherical, and as the magnetic activity decreases (with age) they are not detected anymore in older disks. Moreover, the X-ray emission of the debris disks with detected H I(7-6) lines almost reaches the saturation level for chromospheric emission ($L_X/L_{star} \sim 10^{-3}$, e.g., Patten & Simon 1996, Figure 15, top-right panel). This saturation level indicates that the chromospheric radiation emitted from the star cannot exceed a given fraction of the total stellar flux, and this limit is almost reached in all the observed debris disks, favoring again a chromospheric origin of the H I lines. Another test to check whether or not H I lines in debris disks are from chromospheric activity is shown in the bottom-left panel of Fig. 15, where we plot the stellar chromospherical activity indicator $R^{'}_{HK}$ (collected from White et al. 2007). This indicator measures the core emission in the Ca II H and K lines, and the larger is the value, the more chromospherically active is the star (Noyes et al. 1984)[7]. For the debris disks where this value has been measured there is no significant difference in terms of range covered by $R^{'}_{HK}$ as a function of H I line luminosity, showing that stars with the same chromospheric activity (similar $R^{'}_{HK}$ value) may or may not have detected H I line. On the other hand, the object with strongest

[7] we note the reader that the $R^{'}_{HK}$ index may itself vary with time along the magnetic cycle of the star.

H I line has the largest R'_{HK} value, which would support chromospheric origin in this case. However, the sample is limited to only three objects, and statistical studies are not possible.

We also speculate on the possibility that, as for full and transitional disks, the detection of the mid-IR H I lines in the *Spitzer* spectra of debris disks might trace accretion at very low levels. In fact, Fig. 15, bottom-right panel shows that the H I line is detected in the youngest systems from our sample, for which low level of accretion may be still ongoing. While multiplicity studies are not complete for debris disks, it is intriguing to note that the two debris disks with a confirmed companion close enough to contribute to the observed *Spitzer* spectrum (see Table A1 in Appendix A), have mid-IR hydrogen line detections. This raises yet another possibility that the H I(7-6) line observed in debris disks is due to an accreting or chromospherically active companion, instead of the debris disk object itself. However, this remains a speculation at this point given the low number of detections.

In summary, even if a chromospheric origin appears the most likely based on the tests carried out so far, accretion cannot be ruled out. Only higher spectral resolution will be able to pin down the origin of mid-IR hydrogen lines.

5. SUMMARY AND OUTLOOK

We have re-reduced archival *Spitzer*/IRS spectra of 114 objects in different evolutionary stages, from full to transitional to debris disks, and we have investigated the origin of the H I mid-IR lines. Our main findings are as follows.

1. After correcting for the disk water contamination, we detect H I(7-6) line in 26 full disks, 12 transitional and 8 debris disks. The fainter H I(9-7) line is detected in 6 full, 3 transitional and 2 debris disks.

2. We find H I(7-6) luminosities similar to the [Ne II] 12.81 μm luminosities. These large luminosities exclude that the H I(7-6) line traces the same hot disk surface probed via the [Ne II] line.

3. Case B models cannot reproduce the observed H I(9-7)/H I(7-6) ratios except for T<3000K. On the other hand, KF models reproduce the observed ratios for reasonable assumption of temperatures and hydrogen column densities (n_H). Using the KF models the n_H is fairly well constrained between $10^{10} < n_H < 10^{11}$cm^{-3} but the temperature is not.

4. For the subset of full and transitional disks we report a positive correlation between the H I(7-6) line luminosity and the accretion luminosity. This trend, together with the results shown in point 3 suggest an origin of these lines from gas accreting onto the star.

5. A pure chromospheric origin of the mid-IR H I lines, can only be tested for sources with T_{eff} <4100 K (40% of the total sample). For this subset of objects we find that the majority of them are not contaminated by chromospheric emission at a significant level.

6. We report the first detection of H I lines in *Spitzer* spectra of debris disks, which occurs only the in the youngest systems studied here (< 20 Myr). A chromospheric origin of these lines seems likely, but it is not possible to definitively rule out either a long-lasting accretion signature nature, or the presence of a non-resolved accreting companion.

Ground-based high-resolution spectroscopy will enable testing this origin. Extending accretion indicators at mid-IR wavelengths may enable measuring mass accretion rates in less evolved, still embedded Class I objects (where the star is still surrounded by a remnant infall envelope and accretion disk). Still, care should be taken in converting the mid-IR H I line luminosities into mass accretion rate, because the envelope surrounding Class I sources could absorb part of the emission. More interestingly and on a speculative base, if the mid-IR H I lines were confirmed as accretion indicators in debris disks, these lines may be used to extend mass accretion rate measurements to very low values. If the detected H I lines are indeed tracing accretion, the luminosities we measure for the 8 debris disks correspond to mass accretion rates $\lesssim 10^{-10} M_{\odot}$/yr. Optical and UV accretion diagnostics are not sensitive to such low mass accretion rates for sun-like stars (e.g., Manara et al. 2013).

Finally, extending accretion indicators to the mid-IR will enable simultaneous observations of the [Ne II] line (the only confirmed photoevaporative wind indicator) and the H I line (an accretion indicator), making possible a direct comparison of the two most efficient disk dispersal mechanisms, photoevaporation and viscous accretion (Alexander et al. 2014).

The authors thank Catherine Espaillat and Lynne Hillenbrand for providing the optical spectra and physical parameters of a few objects, and John Kwan for providing the mid-IR hydrogen line ratios. E.R. is supported by the NASA's Astrophysics Data Analysis Program research grant to I.P. (ID: NNX11AG60G).

REFERENCES

Alcalà, J.M., Natta, A., Manara, C., et al. 2014, A&A, 561, 2A
Alexander, R., Pascucci, I., Andrews, S. et al. 2014 Protostars and Planets VI, University of Arizona Press (2014), eds. H. Beuther, R. Klessen, C. Dullemond, Th. Henning (arXiv1311.1819)
Appenzeller, I., Krautter, J. & Jankovics, I. 1983, A&AS, 53, 291A
Baker, J. G. & Menzel, D. H. 1938, ApJ, 88, 52B
Baldovin-Saavedra, C., Audard, M., Güdel, M. et al. 2011, A&A, 528A, 22B
Baldovin-Saavedra, C., Audard, M., Carmona, A. et al. 2012, A&A, 543A, 30B
Baliunas, S., Sokoloff, D., Soon, W. 1996, ApJL, 457, 99
Banzatti et al. 2013, PhD Thesis: âĂIJWater vapor in protoplanetary disksâĂİ
Bary, J. S., Matt, S. P., Skrutskie, M. F. et al. 2008, ApJ, 687, 376B
Basri, G. & Batalha, C. 1990, ApJ, 363, 654B
Biller, B., Close, L., Masciadri, E., et al. 2007, ApJS, 173, 143B
Brown, J.M., Blake, G.A., Qi, C. et al. 2009, ApJ, 704, 496
Calvet, N. & Hartmann, L. 1992, ApJ, 386, 239C
Calvet, N., D'Alessio, P., Hartmann, L., et al. 2002, ApJ, 568, 1008
Calvet, N., Muzerolle, J., Briceño, C. et al. 2004, AJ, 128, 1294C
Carpenter, J. M. & Stauffer, J. 2003, FEPS Memo No.4 http://feps.as.arizona.edu/index.html
Carr , J. & Najita, J. 2008, Science, 319, 1504C
Carr , J. & Najita, J. 2011, ApJ, 733, 102
Casali, M. M. & Eiroa, C. 1996, A&A, 306, 427C
Chen, C.H., Mittal, T., Kuchner, M. et al. 2014, ApJS, 211, 25
Cieza, L., Schreiber, M., Romero, G., et al. 2010, ApJ, 712, 925
Cohen, M. & Kuhi, L. V. 1979, ApJS, 41, 743C
Costigan, G., Scholz, A., Stelzer, B. et al. 2012, MNRAS, 427, 1344C
Dent, W. R. F., Thi, W. F., Kamp, I., et al. 2013, PASP, 125, 477D
Duchene, G., Monin, J., Bouvier, J. & Menard, F. 1999, A&A, 351, 954D
Dutrey, A., Semenov, D., Chapillon, E., et al. 2014, Protostars and Planets VI, University of Arizona Press (2014), eds. H. Beuther, R. Klessen, C. Dullemond, Th. Henning (arXiv1402.3503)
Edwards, S., Kwan, J., Fischer, W. et al. 2013, ApJ, 778, 148E
Ercolano, B., Drake, J. J., Raymond, J. C. & Clarke, C. C. 2008, ApJ, 688, 398E
Ercolano, B. & Owen, J. 2010, MNRAS, 406, 1553E

Espaillat, C., Ingleby, L., Hernàndez, J., et al. 2012, ApJ, 747, 103
Espaillat, C., Ingleby, L., Furlan, E., et al. 2013, ApJ, 762, 62E
Evans, T.M., Ireland, M.J., Kraus, A.L., et al. 2012 ApJ, 744, 120
Fang, M., van Boekel, R., Wang, W., et al. 2009, A&A, 504, 461F
Feigelson, E.; Townsley, L.; Güdel, M. & Stassun, K. 2007, prpl.conf, 313F
Fernandez, M., Ortiz, E., Eiroa, C. & Miranda, L. F. 1995, A&AS, 114, 439F
Folha, D. F. M. & Emerson, J. P. 2001, A&A, 365, 90F
Furlan, E., Hartmann, L., Calvet, N. et al. 2006, ApJS, 165, 568F
Furlan, E., Luhman, K., Espaillat, C., et al. 2011, ApJS 195, 3
Giampapa, M. S., Calvet, N., Imhoff, C. L. & Kuhi, L. V. 1981, ApJ, 251, 113G
Gray, R. O., Corbally, C. J., Garrison, R. F. et al. 2006, AJ, 132, 161G
Güdel, M., Lahuis, F., Briggs, K. R. et al. 2010, A&A, 519A, 113G
Guenther, E. W. & Emerson, J. P. 1997, A&A, 321, 803G
Gullbring, E., Hartmann, L., Briceño, C. & Calvet, N. 1998, ApJ, 492, 323G
Johns-Krull, C. 2007, ApJ, 664, 975J
Hartigan, P., Edwards, S. & Ghandour, L. 1995, ApJ, 452, 736H
Hartmann, L., Avrett, E. H., Loeser, R. & Calvet, N. 1990, ApJ, 349, 168H
Henry, T.J., Soderblom, D.R., Donahue R.A., Baliunas S.L. 1996, AJ, 111, 439
Herbig, G. H. & Bell, K. 1988, Third catalog of emission-line stars of the Orion population, Lick Observatory Bulletin 1111,
Herbst, W. 2008, Handbook of Star Forming Regions Vol II, Astronomical Society of the Pacific.
Herczeg, G., Najita, J., Hillenbrand, L. & Pascucci, I. 2007, ApJ, 670, 509H
Hillendrand, L., Carpenter, J., Kim, S.J., et al. 2008, ApJ, 677, 630
Higdon, S. J. U., Devost, D., Higdon, J. L., et al. 2004, PASP, 116, 975
Hollenbach, D., & Gorti, U. 2009, ApJ, 703, 1203
Houck, J., Roellig, T. L., van Cleve, J., et al. 2004, ApJS, 154, 18H
Hughes, J. & Hartigan, P. 1992, AJ, 104, 680H
Hummer, D. G. & Storey, P. J. 1987, MNRAS, 224, 801H
Keane, J. T., Pascucci, I., Espaillat, C., et al. 2014, ApJ, 787, 153K
Kelly, B. C. 2007, ApJ, 665, 1489K
Kenyon, S. J. & Hartmann, Lee 1995, ApJS, 101, 117K
Kenyon, S. J., Brown, D., Tout, C. & Berlind, P. 1998, AJ, 115, 2491K
Kraus, A., Ireland, M., Martinache, F. & Hillenbrand, L. 2011, ApJ, 731, 8K
Kraus, A. & Ireland, M. 2012, ApJ, 745, 5K
Kwan, J. & Fischer, W. 2011, MNRAS, 411, 2383K
Ingleby, L., Calvet, N., Herczeg, G., et al. 2013, ApJ, 767, 112I
Lafrenière, D., Jayawardhana, R., Brandeker, A., et al. 2008, ApJ, 683, 844L
Lafrenière, D., Jayawardhana, R., van Kerkwijk, M.H., et al. 2014, ApJ, 785, 47L
Leinert, C., Zinnecker, H., Weitzel, N. et al. 1993, A&A, 278,m 129L
Levreault, R. 1988, ApJ, 330, 897L
Luhman, K. L., Stauffer, J.R., Muench, A. A. et al. 2003, ApJ, 593, 1093L
Luhman, K.L, Stauffer, J.R., & Mamajek, E.E., 2005, ApJ, 628, L69
Lahuis, F., van Dishoeck, E., Blake, G., et al. 2007, ApJ, 665, 492L
Mamajek, E., Meyer, M., Hinz, P. et al. 2004, ApJ, 612, 496M
Mamajek, E., Meyer, M. & Liebert, 2002, AJ, 124, 1670
Manara, C.F., Testi, L., Rigliaco, E. et al. 2013, A&A, 551, 107
Manara, C.F., Testi, L., Natta, A., et al. 2014, A&A, 568A, 18M
Manoj, P., Kim, K. H., Furlan, E. et al. 2011, ApJS, 193, 11M
Martin, S. C. 1996, ApJ, 470, 537M
Mathis, J. S. 1990, ASPC, 12, 63M
McCabe, C., Ghez, A. M., Prato, L., et al. 2006, ApJ, 636, 932M
Meijerink, R., Pontoppidan, K. M., Blake, G. A., et al. 2009, ApJ, 704, 1471M
Merin, B., Brown, J., Oliveira, I. et al. 2010, ApJ, 718, 1200M
Metchev, S.r A. & Hillenbrand, L. 2009, ApJS, 181, 62M
Meyer, M., Hillenbrand, L., Backman, D., et al. 2006, PASP, 118, 1690M
Muzerolle, J., Hartmann, L. & Calvet, N. 1998, AJ, 116, 455M
Muzerolle, J., Calvet, N. & Hartmann, L. 2001, ApJ, 550, 944M
Muzerolle, J., Allen, L., Megeath, S., et al. 2010, ApJ, 708, 1107M
Najita, J., Carr, J., Strom, S., et al. 2010, ApJ, 712, 274
Natta, A., Testi, L. & Randich, S. 2006, A&A, 452, 245N
Nguyen, D.C., Brandeker, A., van Kerkwijk, M.H. & Jayawardhana, R. 2012, ApJ, 745, 119
Noyes, R. W., Hartmann, L. W., Baliunas, S. L., et al. 1984, ApJ, 279, 763N
Pascucci, I., Gorti, U., Hollenbach, D., et al. 2006, ApJ, 651, 1177P
Pascucci, I., Hollenbach, D., Najita, J., et al. 2007, ApJ, 663, 383
Pascucci, I. & Sterzik, M. 2009, ApJ, 702, 724P
Pascucci, I., Herczeg, G., Carr, J. S. & Bruderer, S. 2013, ApJ, 779, 178P
Patten, B. & Simon, T. 1996, ApJS, 106, 489P
Petrov, P. P., Kurosawa, R., Romanova, M. M., et al. 2014, MNRAS, 442, 3643P
Pinte, C., Padgett, D., Ménard, F., et al. 2008, A&A, 489, 633
Pontoppidan, K., & Dullemond, K. 2005, A&A, 435, 595
Pontoppidan, K., Salyk, C., Blake, G. & K´aufl, H. 2010, ApJL, 722, 173
Pontoppidan, K., Salyk, C., Bergin, E., et al. 2014, Protostars and Planets VI, University of Arizona Press (2014), eds. H. Beuther, R. Klessen, C. Dullemond, Th. (arXiv1401.2423)
Prato, L., Greene, T. P. & Simon, M. 2003, ApJ, 584, 853P
Preibisch, T., Brown, A., Bridges, T., et al., 2002, AJ, 124, 404
Ratzka, T., Köhler, R. & Leinert, Ch. 2005, A&A, 437, 611
Ratzka, T., Leinert, C., Henning, T., et al. 2007, A&A, 471, 173R
Rebull, L. M., Padgett, D. L., McCabe, C. et al. 2010, ApJS, 186, 259R
Reipurth, B. & Zinnecker, H. 1993, A&A, 278, 81R
Reipurth, B., Pedrosa, A. & Lago, M. 1996, A&AS, 120, 229R
Rigliaco, E., Natta, A., Randich, S. & Sacco, G. 2009, A&A, 495L, 13R
Rigliaco, E., Natta, A., Testi, L., et al. 2012, A&A, 548A, 56R
Riviere-Marichalar, P., Ménard, F., Thi, W. F., et al. 2012, A&A, 538L, 3R
Rothman, L. S., Gordon, I. E., Barbe, A., et al. 2009, JQSRT, 110, 533R
Sacco, G. G., Flaccomio, E., Pascucci, I. et al. 2012, ApJ, 747, 142S
Salyk, C., Pontoppidan, K., Geoffrey A. et al. 2008, ApJ, 676L, 49S
Salyk, C., Pontoppidan, K. M., Blake, G. A. et al. 2011, ApJ, 731, 130S
Salyk, C., Herczeg, G., Brown, J., et al. 2013, ApJ, 769, 21S
Siess, L., Dufour, E. & Forestini, M. 2000, A&A, 358, 593S
Silverstone, M. D., Meyer, M. R., Mamajek, E. E., et al. 2006, ApJ, 639, 1138S
Storey, P. J. & Hummer, D. G. 1995, MNRAS, 272, 41S
Strom, K. M., Strom, S. E. & Margulis, M. 1989, ESOC, 33, 423S
Testi, L., Birnstiel, T., Ricci, L., et al. 2014, Protostars and Planets VI, University of Arizona Press (2014), eds. H. Beuther, R. Klessen, C. Dullemond, Th. (arXiv1402.1354)
Torres, C. A. O., Quast, G. R., Melo, C. H. F., & Sterzik, M. F. 2008, Handbook of Star Forming Regions, Volume II: The Southern Sky ASP Monograph Publications, Vol. 5. Edited by Bo Reipurth, p.757
Uchida, K. I., Calvet, N., Hartmann, L., et al., 2004, ApJS, 154, 439
van Boekel, R., Güdel, M. Henning, T., et al. 2009, A&A, 497, 137V
Walter, F. M. 1986, ApJ, 306, 573W
Walter, F. M. 1992, AJ, 104, 758
White, R. & Ghez, A. 2001, ApJ, 556, 265W
White, R. J. & Hillenbrand, L. 2005, ApJ, 621L, 65W
White, R. J.; Gabor, J. M. & Hillenbrand, L. 2007, AJ, 133, 2524W
Wilking, B., Meyer, M., Robinson, J. & Greene, T. 2005, AJ, 130, 1733W
Woitas, J., Leinert, Ch. & Köhler, R. 2001, A&A, 376, 982W
Wright, J.T., Marcy, G.W., Butler, R.P. & Vogt, S.S. 2004, ApJS, 152, 261
Zuckerman, B., Song, & Webb 2001, ApJ, 559, 388
Zuckerman, B. & Song, I. 2004, ARA&A, 42, 685Z

APPENDIX

APPENDIX

In Figure A1 we show the H I(7-6) line for all the full and transitional disks where the line is detected. The H I(7-6) line profile for debris disks are shown in Figure 14. In Table A1 we report the source properties, and Table A2 report the mid-IR line fluxes, errors and continuum levels around the three line of interest.

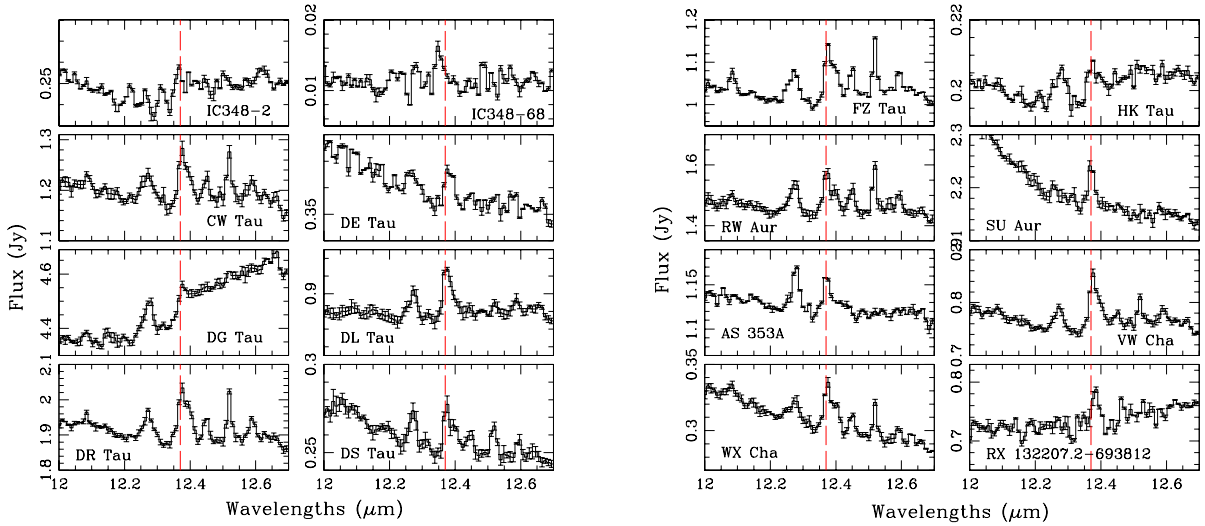

FIG. A1.— IRS spectra around the HI(7-6) line for the objects where the line is detected

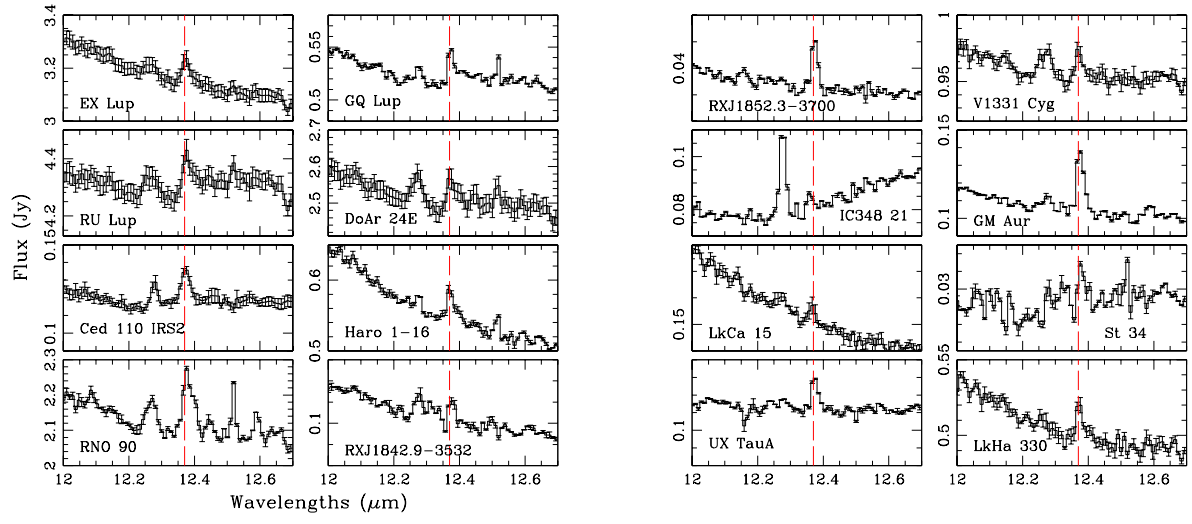

Fig. A1. — continued

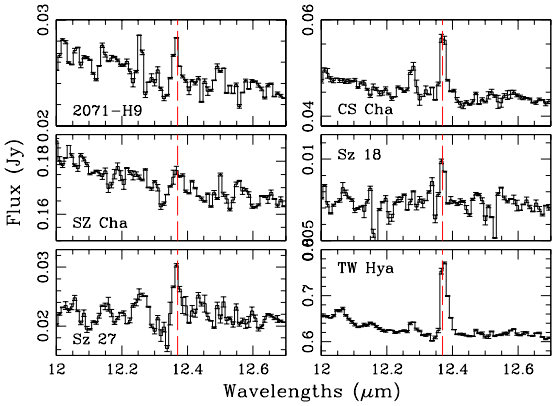

Fig. A1. — continued.

TABLE A1
SOURCE PROPERTIES

Name	Association	Distance (pc)	SpTy	A_V	T_{eff} (K)	M_{star} ($M_\odot$)	L_{star} ($L_\odot$)	R_{star} ($R_\odot$)	HαEW (Å)	L_{acc} ($L_\odot$)	Reference
Full disks											
IC348-2	IC 348	315	A2	3.8	8970	2.80	57.1	3.1	···	···	18,11
IC348-6	IC 348	315	G3	3.9	5830	2.40	16.6	4.0	···	···	18,11
IC348-31	IC 348	315	G6	8.6	5700	1.60	5.00	2.3	···	···	18,11
IC348-37	IC 348	315	K6	2.8	4200	0.90	1.30	2.2	···	···	18,11
IC348-55	IC 348	315	M0.5	8.5	3850	0.60	1.00	2.2	···	···	18,11
IC348-68	IC 348	315	M3.5	2.1	3740	0.30	0.50	2.0	···	···	18,11
04216+2603	Taurus	140	M0	···	3500	0.28	0.02	0.3	···	···	14,21
04385+2550	Taurus	140	M0	9.3	3850	0.57	3.67	4.0	20.0	0.50	14,21
AA Tau*	Taurus	140	K7	0.9	4060	0.73	1.38	2.3	37.1	0.07	14,9
BP Tau	Taurus	140	K7	0.5	4060	0.73	1.62	2.4	40.1	0.07	14,9
CW Tau*	Taurus	140	K3	2.2	4730	1.15	0.76	1.3	134.6	0.30	14,49
CX Tau	Taurus	140	M2.5	0.8	3490	0.36	0.62	2.0	19.8	0.003	14,9
CY Tau*	Taurus	140	M1	0.9	3705	0.47	0.71	1.9	69.5	0.06	14,9
DD Tau ^{m,*}	Taurus	140	M3	0.4	3415	0.29	0.13	1.0	181.8	0.05	14,49, 9
DE Tau	Taurus	140	M1	1.6	3705	0.46	1.47	2.8	54.0	0.23	14,49, 9
DG Tau	Taurus	140	K6	1.4	4205	0.92	1.15	1.9	84.0	0.17	14,49
DK Tau^{m,*}	Taurus	140	K7	1.4	4060	0.74	1.32	2.2	19.4	0.02	14,9,44
DH Tau*	Taurus	140	M0	1.0	3850	0.56	0.76	1.8	53.4	0.03	14,9
DL Tau*	Taurus	140	K7	2.0	4060	0.75	1.16	2.2	105.0	0.62	14,49
DN Tau*	Taurus	140	M0	0.4	3850	0.55	1.62	2.7	11.9	0.016	14,49
DO Tau*	Taurus	140	M0	2.2	3850	0.56	1.05	2.2	100.0	0.19	14,49
DP Tau^{m,*}	Taurus	140	M0.5	0.9	3850	0.56	0.85	1.9	85.4	0.05	14,9
DQ Tau^{a,*}	Taurus	140	M0	0.5	3850	0.56	0.93	2.0	112.9	0.04	14,9
DR Tau*	Taurus	140	K5	0.5	4350	1.16	0.96	1.9	106.0	0.49	14,49
DS Tau*	Taurus	140	K5	0.9	4350	1.10	0.68	1.3	58.7	0.16	14,49
FM Tau*	Taurus	140	M0	0.9	3850	0.57	0.52	1.5	70.9	0.02	14,9
FN Tau	Taurus	140	M5	1.4	3125	0.22	0.79	2.8	24.7	0.007	14,9
FT Tau*	Taurus	140	M3	3.8	3415	0.31	0.16	1.0	254.3	0.49	14,9,40
FZ Tau*	Taurus	140	M0	2.7	3850	0.57	0.50	1.4	200.0	0.26	14,49
HK Tau^m	Taurus	140	M0.5	3.0	3850	0.56	1.12	2.2	29.3	0.028	14,9
HN Tau^{m,*}	Taurus	140	K5	1.2	4350	0.78	0.22	0.8	163.0	0.15	14,49
IP Tau	Taurus	140	M0	0.5	3850	0.59	0.17	0.9	11.0	0.005	14,49
RW Aur^{m,*}	Taurus	140	K3	0.4	4730	1.48	1.60	1.8	76.0	0.924	14,49
SU Aur	Taurus	140	G2	0.9	5860	1.85	8.90	2.7	3.5	0.14	14,9
UY Aur^m	Taurus	140	K7	1.1	3850	0.60	0.91	2.1	72.8	1.02	14,9,49
AS 353A^m	Perseus	150	M3	2.1	3415	0.32	0.68	2.2	124.5	1.60	38,9
LkHa326	Perseus	250	M0	3.1	3800	0.49	0.05	0.5	52.7	0.10	6,9
2071-H13/ NGC2068	NGC2068	400	K1	2.9	5080	1.68	2.63	2.0	36.7	0.42	11
2071-S1/ NGC2068	NGC2068	400	K4	4.1	4600	1.60	4.10	3.1	3.7	0.005	11
RX J1111.7-7620^m	Cha	160	K1	1.5	5080	1.78	3.09	2.2	7.6	0.04	43,48
SX Cha^{m,*}	Cha	160	M0.5	1.1	3850	0.57	0.61	1.6	33.2	0.02	15,16
SZ50	Cha	160	M3	2.1	3350	0.90	0.78	2.5	46.0	0.015	15,20
TWCha	Cha	160	M0	1.2	3850	0.56	3.10	3.7	28.3	0.04	15,16
VW Cha^{m,*}	Cha	160	K5	2.4	4350	1.14	4.02	3.3	71.7	0.81	15,42
VZ Cha*	Cha	160	K6	0.5	4205	0.93	0.84	1.6	71.4	0.099	15,42

TABLE A1
SOURCE PROPERTIES

WX Cha[m,*]	Cha	160	K7	2.1	4060	0.77	0.77	1.8	65.5	0.07	15,1
XX Cha[m,*]	Cha	160	M2	0.6	3560	0.37	0.18	1.1	133.5	0.03	15,1
Hen-3-600A	TWHya	56	M3	0.0	3415	0.26	0.06	0.6	21.8	0.007	46
TWA10	TWHya	100	M2	0.0	5500	0.90	0.60	1.0	···	···	55
1RXS J132207.2-693812	LCC	86	K1	0.6	5035	1.23	1.14	1.4	19.5	0.07	43,51
EX Lup*	Lupus	190	M0	0.0	3850	0.55	1.31	2.4	31.3	0.06	26,42
GQ Lup*	Lupus	190	K7	0.4	4060	0.76	4.53	4.1	31.7	0.31	26,42
HT Lup[m]	Lupus	190	K3	0.0	4730	1.85	4.00	2.8	7.3	0.11	26,42,54
RU Lup*	Lupus	190	K7	0.7	4060	0.74	1.28	2.2	136.0	0.69	26,42
1RXS J161411.0-230536[m]	Upper Scorpius	140	K0	1.1	5250	1.62	2.95	2.0	···	···	43,29
HD 143006	Upper Scorpius	169	G7	0.6	5800	1.12	3.30	1.7	10.7	0.19	43,29
DoAr 24E[m,*]	ρOphiucus	160	G7	6.1	5630	2.15	10.75	3.3	7.1	0.24	15,53
f DoAr 25*	ρOphiucus	160	K5	2.9	4350	1.11	2.19	2.3	12.0	0.05	8,53
SR21[m]	ρOphiucus	125	G2.5	9.0	5950	2.67	28.0	4.7	···	···	38
WaOph6*	ρOphiucus	160	K6	1.0	4205	0.90	1.46	2.3	35.0	0.02	26,47
Ced110-IRS4	ρOphiucus	160	K2	···	4800	0.85	0.40	0.9	···	···	37
Ced110-IRS2	ρOphiucus	160	K3	3.3	4730	2.23	9.64	4.4	···	···	15
Haro 1-16*	ρOphiucus	160	K3	1.2	4730	1.80	3.39	2.7	59.0	0.24	14,9
RNO 90*	ρOphiucus	160	G5	1.0	5770	1.28	2.74	1.6	76.0	0.47	26,28
EC 82	Serpens	415	K7	1.0	4060	0.75	3.21	3.3	8.0	0.03	26,9
RX J1842.9-3532	CrA	136	K2	1.1	4900	1.33	1.29	1.5	27.2	0.06	43,51
RX J1852.3-3700	CrA	136	K3	1.0	4730	1.27	1.00	1.5	27.4	0.06	43,51
V1331Cyg	Cyn	550	G8	0.0	5500	2.81	21.0	4.8	48.4	2.01	9,35
Transitional disks											
IC348-21	IC 348	315	K0	4.7	5250	1.60	3.80	2.4	6.4	0.08	11
IC348-67	IC 348	315	M0.75	2.0	3720	0.50	0.50	1.8	32.5	0.03	11
IC348-72	IC 348	315	M2.5	3.0	3580	0.40	0.70	2.1	2.0	0.0007	11
IC348-133	IC 348	315	M5	3.6	3200	0.20	0.20	1.5	···	···	11
DM Tau	Taurus	140	M1	0.0	3705	0.47	0.37	1.3	138.7	0.046	14,21
FP Tau	Taurus	140	M5	0.3	3125	0.22	0.62	2.5	38.5	0.001	14,21
GM Aur	Taurus	140	K3	1.2	4730	1.27	1.00	1.5	96.5	0.58	14,21
LkCa 15[m]	Taurus	140	K5	1.0	4300	1.06	0.74	1.5	13.0	0.027	14,21
St 34[m]	Taurus	140	M3	0.2	3415	0.24	0.01	0.3	51.6	0.016	26,50
UX Tau A[m]	Taurus	140	K5	0.3	4350	1.17	0.91	1.9	9.5	0.03	14,17
V836Tau	Taurus	140	K7	0.9	4060	0.81	0.34	1.2	55.0	0.16	14,21,34
LkHa 330	Perseus	250	G3	1.8	5830	1.25	2.78	1.5	20.3	0.59	3,13
2071-H9/ NGC2068	NGC2068	400	K2	1.6	5250	1.41	2.03	1.7	1.2	0.004	11
CHX 22 (T54)[m]	Cha	160	G8	1.2	5520	1.69	4.63	2.2	···	···	15,48, 34
CS Cha	Cha	160	K6	0.8	4205	0.90	1.50	2.3	54.3	0.39	15, 42
SZ Cha[m]	Cha	160	K0	1.9	5250	1.40	1.90	1.7	···	···	15, 42
Sz 18 (T25)	Cha	160	M2.5	1.6	3560	0.38	0.32	1.4	8.0	0.003	15,30
Sz 27 (T35)	Cha	160	K8	3.5	4060	0.80	0.47	1.2	100.0	0.08	15,30
TW Hya	TWHya	56	M0	1.0	3850	0.57	0.64	1.7	194.0	0.09	4,42
IM Lup	Lupus	190	M0	0.7	3850	0.56	3.52	3.9	4.7	0.02	36,42
DoAr 21	ρOphiucus	160	K1	6.6	5080	2.20	27.3	6.7	1.5	0.12	33,31
Debris disks											
1RXS J121236.4-552037	LCC	108	K0	0.2	5150	0.90	0.50	0.9	···	···	5, 7
1RXS J122233.4-533347	LCC	124	G0	0.3	5860	1.24	2.23	1.3	···	···	5, 7
1RXS J130153.7-530446	LCC	108	K2	0.2	4700	0.82	0.30	0.8	···	···	5, 7
HD119269	LCC	85	G4	0.1	5700	1.07	1.31	1.2	···	···	5, 7
1RXS J133758.0-413448	UCL	98	K0	0.3	5250	0.90	0.68	0.9	···	···	5, 7
1RXS J161458.4-27501	Upper Scorpius	114	G5	0.6	5250	0.90	0.70	1.0	···	···	43,51
HD 142361[m]	Upper Scorpius	101	G3	0.5	5830	1.72	7.12	2.5	···	···	5, 7
RX J1600.6-2159	Upper Scorpius	160	G9	0.8	5410	1.66	3.77	2.1	···	···	43,51
RX J1612.6-1859[m]	Upper Scorpius	127	K0	1.5	5250	1.50	2.40	1.8	···	···	19,51
HD 35850	βPictoris	26.5	F7	0.0	6000	1.20	1.78	1.2	···	···	5, 7
V343 Nor[m]	βPictoris	38	K0	0.0	5250	0.90	0.67	0.9	···	···	5
HD19668	AB Dor	40	G8/K0	0.0	5500	0.90	0.60	0.8	···	···	5, 7
HD25457	AB Dor	19	F7	0.2	6000	1.20	2.50	1.5	···	···	5, 7
HD37484	Columba	60	F3	0.1	6740	1.30	3.90	1.5	···	···	5, 7
HD12039[m]	Tuc-Hor	42	G4	0.2	6000	1.00	1.00	0.9	···	···	5, 7
HD202917	Tuc-Hor	46	G7	0.1	5750	0.90	0.70	0.8	···	···	5, 7
HD 141943	Field	67	G0	0.1	6030	1.55	6.19	2.2	···	···	5
HD377	Field	39.6	G2	0.2	6250	1.00	1.50	1.0	···	···	5, 7
HD17925	Field	10	K1	0.0	5080	0.92	0.55	0.9	···	···	5, 7
HD32297	Field	112	A0	0.2	8000	1.90	6.20	1.3	···	···	5, 7
HD61005	Field	34	G8	0.1	5759	0.90	0.60	0.8	···	···	5, 7
HD69830	Field	13	G8	0.0	5500	0.90	0.60	0.85	···	···	5, 7
HD134319	Field	44	G5	0.0	5770	1.00	0.72	0.8	···	···	5, 7
HD216803	Field	8	K4	0.0	4600	0.66	0.19	0.7	···	···	5, 7
AOMen	Field	39	K3	0.0	4435	0.70	0.26	0.9	···	···	5

TABLE A1
SOURCE PROPERTIES

REFERENCES. — (1) Appenzeller et al. 1983; (2) Biller et al. 2007; (3) Brown et al. 2009; (4) Calvet et al. 2002; (5) Carpenter & Stauffer 2003 (6) Casali & Eiroa 1996 (7) Chen et al. 2014 (8) Cieza et al. 2010; (9) Cohen & Kuhi 1979; (10) Duchene et al. 1999; (11) Espaillat et al. 2012; (12) Evans et al. 2012; (13) Fernandez et al. 1995; (14) Furlan et al. 2006; (15) Furlan et al. 2011; (16) Guenther & Emerson 1997; (17) Herbig & Bell 1988; (18) Herbst, W. 2008; (19) Hillenbrand et al. 2008; (20) Hughes & Hartigan 1992 (21) Kenyon et al. 1998; (22) Kraus et al. 2011; (23) Kraus & Ireland 2012; (24) Lafreniere et al. 2008; (25) Lafreniere et al. 2014; (26) Lahuis et al. 2007; (27) Leinert et al. 1993; (28) Levreault 1988; (29) Mamajek et al. 2004; (30) Manoj et al. 2011 (31) Merin et al. 2010; (32) Metchev & Hillenbrand 2009; (33) Muzerolle et al. 2010; (34) Nguyen et al. 2012; (35) Petrov et al. 2014 (36) Pinte et al. 2008; (37) Pontoppidan & Dullemond 2005; (38) Prato et al. 2003; (39) Ratzka et al. 2005; (40) Rebull et al. 2010; (41) Reipurth & Zinnecker 1993 (42) Reipurth et al. 1996; (43) Silverstone et al. 2006; (44) Strom et al. 1989 (45) Torres et al. 2008; (46) Uchida et al. 2004 (47) Walter 1986; (48) Walter 1992; (49) White & Ghez 2001; (50) White & Hillenbrand 2005; (51) White et al. 2007; (52) White et al. in prep; (53) Wilking et al. 2005; (54) Woitas et al. 2001 (55) Zuckerman & Song 2004

NOTE. — Objects marked with * are water-contaminated. ^{a}=Spectroscopic Binary treated as single star (22). Stars marked with ^{m} are binary or multiple systems with the following separation: AS 353A 5.6″ (22), CHX 22 0.25″ (24), DD Tau 0.56″ (49), DK Tau 2.4″ (22), DoAr 24E 2.05″ (39), DP Tau 0.11″ (22), HD 12039 0.15″ (2) - (this multiplicity has not been confirmed (12)), HD 142361 0.73″ (32) - (this multiplicity has not been confirmed (32, 25)), HK Tau 2.4″ (27), HN Tau 3.1″ (27), HT Lup 2.8″ (54), LkCa15 0.08″ (23), RX J1111.7-7620 0.27″ (24), RX J1612.6-1859 0.21″ (32), 1RXS J161411.0-230536 0.22″ (32), RW Aur 1.4 ″ (22), SR21 6.4″ (41), St 34 1.18″ (52), SX Cha 2.2″ (24), SZ Cha 5.12″ (24), UX TauA 2.7,0.14″ (10), UY Aur 0.89″ (27), V343NOR 10″ (45), VW Cha 0.64,0.10 ″ (24), WX Cha 0.79 ″ (24).

TABLE A2
MID-IR LINE FLUXES, ERRORS AND CONTINUUM LEVEL AROUND THE LINES

Name	[Ne II]			H I(7-6)			H I(9-7)		
	Flux[a]	1σ[a]	cont[b]	Flux[a]	1σ[a]	cont[b]	Flux[a]	1σ[a]	cont[b]
				Full disks					
IC348-2	7.66E-15	1.81E-15	0.24	4.05E-15	7.45E-16	0.25	<6.46E-15	···	0.33
IC348-6	<2.23E-15	···	0.078	<2.73E-15	···	0.077	<1.18E-14	···	0.11
IC348-31	<2.68E-15	···	0.076	<3.43E-15	···	0.067	<3.62E-15	···	0.067
IC348-37	<2.46E-15	···	0.055	<2.22E-15	···	0.059	<2.92E-15	···	0.081
IC348-55	2.16E-15	7.28E-16	0.034	<1.94E-15	···	0.037	<3.31E-15	···	0.052
IC348-68	<1.41E-15	···	0.011	2.68E-15	4.97E-16	0.011	<3.51E-15	···	0.012
04216+2603	<3.41E-15	···	0.20	<4.77E-15	···	0.20	<7.17E-15	···	0.23
04385+2550*	4.33E-15	1.66E-15	0.35	<7.61E-15	···	0.34	<1.08E-14	···	0.38
AA Tau*	1.32E-14	2.14E-15	0.31	<7.61E-15	···	0.32	<1.63E-14	···	0.41
BP Tau*	<5.61E-15	···	0.36	<6.70E-15	···	0.38	<1.80E-14	···	0.51
CW Tau*	<1.71E-14	···	1.13	3.45E-14 (5.73E-14)	4.20E-15	1.18	<3.73E-14	···	1.33
CX Tau	<2.38E-15	···	0.17	<3.01E-15	···	0.17	<5.55E-15	···	0.20
CY Tau*	2.22E-15	9.68E-16	0.15	<4.93E-15	···	0.16	<3.53E-15	···	0.18
DD Tau*	2.02E-14	4.73E-15	0.93	<1.37E-14	···	0.96	<5.02E-14	···	1.14
DE Tau	<5.75E-15	···	0.35	7.81E-15	1.40E-15	0.35	<1.34E-14	···	0.49
DG Tau	2.43E-13	1.13E-14	4.64	4.49E-14	6.49E-15	4.47	<5.44E-14	···	4.52
DK Tau*	<9.78E-15	···	0.78	<2.46E-14	···	0.88	<1.54E-14	···	1.24
DH Tau*	<3.99E-15	···	0.12	<4.01E-15	···	0.12	<1.04E-14	···	0.16
DL Tau*	1.24E-14	2.15E-15	0.87	7.12E-15 (3.24E-14)	2.09E-15	0.88	1.58E-14 (1.84E-14)	2.52E-15	0.93
DN Tau*	3.83E-15	5.38E-16	0.28	<3.22E-15	···	0.29	<2.92E-15	···	0.31
DO Tau*	<1.51E-14	···	1.89	<1.75E-14	···	1.94	<1.76E-14	···	2.17
DP Tau*	1.16E-13	3.63E-15	0.63	<2.42E-14	···	0.66	<2.44E-14	···	0.78
DQ Tau*	9.06E-15	3.33E-15	0.60	<1.14E-14	···	0.61	<1.19E-14	···	0.64
DR Tau*	<2.12E-14	···	1.88	3.46E-14 (1.03E-13)	6.93E-15	1.88	1.69E-14 (4.08E-14)	8.65E-15	2.10
DS Tau*	<6.33E-15	···	0.24	4.23E-15 (1.28E-14)	1.10E-15	0.25	<6.32E-15	···	0.36
FM Tau*	<2.26E-15	···	0.25	<4.85E-15	···	0.27	<6.71E-15	···	0.34
FN Tau	5.44E-15	1.23E-15	0.68	<5.71E-15	···	0.67	<5.59E-15	···	0.83
FT Tau*	5.97E-15	1.45E-15	0.25	<4.54E-15	···	0.26	<1.07E-14	···	0.31
FZ Tau*	<1.75E-14	···	0.98	2.46E-14 (8.65E-14)	3.42E-15	1.02	2.23E-14 (3.17E-14)	7.12E-15	1.15
HK Tau	5.51E-15	1.08E-15	0.20	3.44E-15	7.21E-16	0.20	<4.42E-15	···	0.24
HN Tau*	2.59E-14	4.81E-15	0.95	<1.66E-14	···	1.01	<4.05E-14	···	1.36
IP Tau	<6.22E-16	···	0.013	<8.16E-16	···	0.014	<1.94E-15	···	0.020
RW Aur*	<2.00E-14	···	1.43	1.96E-14 (7.16E-14)	5.92E-15	1.46	<3.23E-14	···	1.76
SU Aur	1.78E-14	3.63E-15	2.14	3.27E-14	3.87E-15	2.17	<7.15E-14	···	3.02
UYAur	<2.49E-14	···	2.36	<3.39E-14	···	2.38	<8.22E-14	···	2.67
AS 353A	1.11E-14	2.50E-15	1.11	1.96E-14	3.07E-15	1.13	<1.80E-14	···	1.26
LkHa326	4.74E-15	1.23E-15	0.33	<8.34E-15	···	0.33	<1.27E-14	···	0.36
2071-H13/ NGC2068	1.01E-15	2.43E-16	0.024	<9.83E-16	···	0.026	<1.71E-15	···	0.038
NGC20682071-S1	<1.97E-15	···	0.046	<1.77E-15	···	0.050	<2.23E-15	···	0.061
RX J1111.7-7620	9.97E-15	1.28E-15	0.22	<5.96E-15	···	0.23	<9.55E-15	···	0.27
SX Cha*	<7.08E-15	···	0.49	<1.34E-14	···	0.51	<1.42E-14	···	0.65
SZ50	<3.20E-15	···	0.20	<4.78E-15	···	0.21	<7.16E-15	···	0.22
TWCha	<4.35E-15	···	0.062	<4.01E-15	···	0.055	<6.63E-15	···	0.042
VW Cha*	3.13E-14	3.50E-15	0.73	3.74E-14 (5.98E-14)	2.79E-15	0.76	1.91E-14 (2.64E-14)	5.18E-15	0.95
VZ Cha*	<5.92E-15	···	0.37	<8.84E-15	···	0.40	<8.61E-15	···	0.46
WX Cha*	<5.08E-15	···	0.28	1.29E-14 (2.62E-14)	1.34E-15	0.30	<1.01E-14	···	0.43
XX Cha*	4.57E-15	7.48E-16	0.13	<5.66E-15	···	0.14	<6.46E-15	···	0.16
Hen-3-600A	<6.62E-15	···	0.099	<4.78E-15	···	0.095	<1.08E-14	···	0.11
TWA10	<2.44E-15	···	0.018	<2.09E-15	···	0.019	<3.05E-15	···	0.022
RX 132207.2-693812	<2.59E-14	···	0.75	3.46E-14	6.13E-15	0.74	3.17E-14	1.23E-14	0.84
EX Lup*	<1.63E-14	···	3.13	1.71E-14 (5.34E-14)	6.85E-15	3.21	<4.43E-14	···	4.12
GQ Lup*	<6.38E-15	···	0.49	4.39E-15 (1.23E-14)	2.29E-15	0.52	<9.91E-15	···	0.65
HTLup	<1.90E-14	···	2.17	<1.96E-14	···	2.21	<5.23E-14	···	2.64
RU Lup*	4.54E-14	8.41E-15	4.29	3.61E-14 (7.74E-14)	8.24E-15	4.36	<6.13E-14	···	4.80
RX J161411.0-230536	6.44E-15	1.36E-15	0.34	<5.69E-15	···	0.35	<7.30E-15	···	0.36
HD143006	<1.08E-14	···	0.69	<1.63E-14	···	0.74	<3.68E-14	···	1.12
DoAr 24E*	1.38E-14	4.20E-15	2.54	1.83E-14 (3.96E-14)	7.58E-15	2.58	<4.14E-14	···	2.96
DoAr 25*	2.87E-15	9.27E-16	0.21	<7.78E-15	···	0.22	<3.84E-15	···	0.24
SR21	<2.84E-14	···	0.79	<3.63E-14	···	0.75	<6.01E-14	···	0.91
Wa Oph6*	8.55E-15	1.83E-15	0.82	<2.25E-14	···	0.82	<1.65E-14	···	0.92
Ced110IRS2	<4.43E-15	···	0.11	1.92E-15	6.24E-16	0.12	<6.97E-15	···	0.15
Ced110-IRS4	2.43E-14	8.57E-16	0.080	<1.84E-15	···	0.070	<1.75E-15	···	0.054
Haro 1-16*	<9.73E-15	···	0.50	1.05E-14 (2.16E-14)	3.42E-15	0.54	<2.43E-14	···	1.05
RNO 90*	2.10E-14	1.08E-14	2.05	5.64E-14 (1.28E-13)	6.22E-15	2.10	3.87E-14 (4.92E-14)	9.83E-15	2.49
EC 82	1.39E-14	3.05E-15	1.32	<1.48E-14	···	1.45	<3.93E-14	···	2.57
RX J1842.9-3532	4.75E-15	7.21E-16	0.092	3.83E-15	7.96E-16	0.10	<5.25E-15	···	0.19
RX J1852.3-3700	8.66E-15	4.28E-16	0.035	4.62E-15	3.26E-16	0.037	<1.74E-15	···	0.055
V1331Cyg	<3.30E-15	···	1.01	1.16E-14	6.24E-16	0.96	<5.64E-15	···	0.95
				Transitional disks					
IC348-21	3.12E-15	5.13E-16	0.088	3.71E-15	9.77E-16	0.081	<5.67E-15	···	0.11
IC348-67	2.40E-15	6.69E-16	0.018	<2.73E-15	···	0.019	<3.43E-15	···	0.023
IC348-72	<2.93E-15	···	0.011	<2.04E-15	···	0.011	<2.12E-15	···	0.012
IC348-133	<2.90E-15	···	0.017	<2.69E-15	···	0.016	<4.85E-15	···	0.023

TABLE A2
MID-IR LINE FLUXES, ERRORS AND CONTINUUM LEVEL AROUND THE LINES

DM Tau	5.45E-15	4.59E-16	0.047	<2.13E-15	···	0.048	<1.56E-15	···	0.055
FP Tau	<4.73E-15	···	0.067	<3.76E-15	···	0.070	<4.31E-15	···	0.078
GM Aur	1.02E-14	7.11E-16	0.097	1.89E-14	9.28E-16	0.10	1.20E-14	1.02E-15	0.17
LkCa 15	3.41E-15	5.54E-16	0.14	2.94E-15	6.71E-16	0.15	<7.89E-15	···	0.27
St 34	1.40E-15	5.66E-16	0.029	1.59E-15	4.68E-16	0.028	<2.12E-15	···	0.029
UX TauA	9.04E-15	9.85E-16	0.11	9.02E-15	8.53E-16	0.11	<4.98E-15	···	0.14
V836Tau	<2.05E-15	···	0.10	<3.61E-15	···	0.11	<3.33E-15	···	0.17
LkHa 330	<4.99E-15	···	0.49	8.84E-15	1.91E-15	0.50	<2.49E-14	···	0.69
2071-H9/ NGC2068	1.21E-15	3.75E-16	0.023	2.44E-15	3.84E-16	0.024	<2.06E-15	···	0.038
CHX 22 (T54)	5.48E-15	9.30E-16	0.032	<2.57E-15	···	0.036	<1.04E-15	···	0.049
CS Cha	3.61E-14	6.12E-16	0.046	6.11E-15	2.53E-16	0.048	3.07E-15	7.43E-16	0.064
SZ Cha	1.48E-14	1.02E-15	0.16	6.10E-15	1.32E-15	0.17	<6.93E-15	···	0.25
SZ 18	7.63E-16	2.33E-16	0.0075	8.68E-16	2.14E-16	0.0073	<2.63E-15	···	0.0080
Sz 27 (T35)	6.32E-15	9.03E-16	0.021	3.03E-15	7.27E-16	0.022	<2.67E-15	···	0.026
TW Hya	5.01E-14	2.07E-15	0.61	7.93E-14	2.00E-15	0.62	3.34E-14	3.64E-15	0.81
IM Lup	7.03E-15	1.54E-15	0.48	<4.58E-15	···	0.49	<6.37E-15	···	0.60
DoAr 21	7.80E-14	2.58E-15	0.65	<1.32E-14	···	0.63	<4.66E-14	···	0.86
				Debris disks					
1RXS J121236.4-55203	<6.09E-16	···	0.014	<8.71E-16	···	0.016	<8.11E-16	···	0.019
1RXS J122233.4-533347	<4.75E-16	···	0.020	8.56E-16	1.95E-16	0.021	<7.81E-16	···	0.026
1RXS J130153.7-53044	<4.95E-16	···	0.0084	<4.67E-16	···	0.0092	<8.19E-16	···	0.011
HD119269	<1.15E-15	···	0.024	<9.33E-16	···	0.026	<1.49E-15	···	0.031
1RXS J133758.0-413448	<6.79E-16	···	0.019	5.44E-16	2.04E-16	0.021	<8.21E-16	···	0.025
1RXS J161458.4-27501	<8.43E-16	···	0.0088	<6.31E-16	···	0.0098	<8.00E-16	···	0.012
HD 142361	<1.59E-15	···	0.040	2.98E-15	1.47E-16	0.043	1.44E-15	2.60E-16	0.052
RX 1600.0-2159	<7.96E-16	···	0.012	1.20E-15	1.91E-16	0.013	<7.63E-16	···	0.015
RX 1612.2-1859	<6.28E-16	···	0.028	9.32E-16	1.53E-16	0.031	<8.60E-16	···	0.036
HD 35850	3.38E-15	1.01E-15	0.26	9.02E-15	9.27E-16	0.27	<6.30E-15	···	0.34
V343Nor	<3.30E-15	···	0.11	4.81E-15	8.09E-16	0.12	<5.64E-15	···	0.15
HD19668	<1.14E-15	···	0.051	<1.62E-15	···	0.056	<2.56E-15	···	0.067
HD25457	<1.86E-14	···	0.53	<1.53E-14	···	0.58	<1.86E-14	···	0.68
HD37484	<2.66E-15	···	0.080	<2.16E-15	···	0.086	<4.47E-15	···	0.10
HD12039	<7.55E-16	···	0.065	<1.31E-15	···	0.071	<1.43E-15	···	0.082
HD202917	<1.94E-15	···	0.044	<3.19E-15	···	0.048	<4.31E-15	···	0.058
HD 141943	<1.27E-15	···	0.074	3.10E-15	4.13E-16	0.080	2.97E-15	4.91E-16	0.094
HD377	<1.79E-15	···	0.088	<1.31E-15	···	0.095	<2.73E-15	···	0.11
HD17925	<3.42E-15	···	0.61	<7.36E-15	···	0.66	<8.26E-15	···	0.78
HD32297	<3.26E-15	···	0.054	<4.28E-15	···	0.053	<5.09E-15	···	0.052
HD61005	<1.49E-15	···	0.066	<1.32E-15	···	0.072	<2.40E-15	···	0.084
HD69830	<4.54E-15	···	0.56	<4.75E-15	···	0.62	<1.05E-14	···	0.81
HD134319	<2.21E-15	···	0.047	<2.55E-15	···	0.051	<2.73E-15	···	0.060
HD216803	<5.66E-15	···	0.74	<7.99E-15	···	0.81	<6.96E-15	···	0.95
AOMen	<1.04E-15	···	0.051	<1.03E-15	···	0.056	<2.08E-15	···	0.065

NOTE. — [a]Fluxes and errors are in erg s^{-1} cm^{-2}. For the detections we report the 1σerror, upper limits are at 3σ. [b] Continua are in Jy. Objects marked with an * refer to water-contaminated disks, and the fluxes reported are already corrected for the water contribution. In parenthesis we report the observed H I fluxes before the water subtraction.